

# 15 Jet Noise Suppression

55-71  
N92-14784

248401

64995

Lead authors

GG100602

P. R. Gliebe  
*General Electric Co.*  
*Cincinnati, Ohio*

J. F. Brausch  
*General Electric Co.*  
*Cincinnati, Ohio*

R. K. Majjigi  
*General Electric Co.*  
*Cincinnati, Ohio*

R. Lee  
*General Electric Co.*  
*Cincinnati, Ohio*

## Introduction

Jet noise suppression has been a technical challenge to the aeronautical engineering community since the introduction of the first-generation turbojet engines nearly 40 years ago. Extensive theoretical and experimental efforts have been expended in the United States and other countries toward solving this problem. The advent of the supersonic transport (SST, i.e., the British-French Concorde) in the late sixties and early seventies sparked a renewed interest in jet noise, particularly supersonic jet noise. Recently, interest in a high-speed civil transport (HSCT) has increased in the United States because of a projected increase in business activity between the United States and the Pacific rim countries in the nineties and beyond. Such an HSCT has to be environmentally acceptable (in terms of noise and pollution) to be a viable candidate. Significant advancements in high-velocity-jet noise reduction have been made since the introduction of the Concorde into the commercial airline service. This chapter briefly discusses the theoretical concepts of jet noise generation and suppression by utilizing a unified aerodynamic and acoustic analysis and enumerating the various jet noise suppression concepts experimentally demonstrated. It also explains the underlying physical mechanisms, so that the knowledge acquired in the past may be utilized for solving the current or future problems of jet noise suppression.

## Theoretical Concepts of Jet Noise Generation and Suppression

During the past 15 years, considerable progress has been made in achieving an understanding of the noise produced by high-velocity jets. This progress is a direct

result of careful and accurate jet noise parametric testing and new theoretical developments (e.g., refs. 1 to 8). From these test results and theoretical developments, a unified theoretical model of jet noise generation and suppression has evolved, and this model has been substantiated with an extensive set of experimental data. This unified jet noise generation and suppression model is summarized in this section. Further details of the theory and the resulting prediction model can be found in references 9 to 12.

The development of the unified jet noise generation and suppression model is based on two primary assumptions: (1) the dominant noise generation mechanisms are the random momentum fluctuations of the small-scale turbulent structure in the mixing regions of the jet plume, and (2) the propagation of this noise to the far-field observer is altered significantly by the surrounding jet flow in which the turbulent eddies are embedded and convecting. This second assumption is often referred to as acoustic-mean-flow interaction. Thus, the proposed model is one in which the jet produces an intrinsic noise intensity spectrum directly relatable to the statistical aerodynamic properties of the jet (i.e., mean velocity and density distributions and local turbulent structure properties such as length scale and intensity), and this intrinsic (or "source") spectrum is modified by the acoustic-mean-flow interaction characteristics of the jet plume itself.

For jets operating at supercritical pressure ratios, one additional noise generation mechanism needs to be included in the unified theory, that is, shock-cell-turbulence interaction, commonly called shock-associated noise. This mechanism plays an important role in jet noise radiation in the forward arc portion of the directivity pattern.

The theoretical prediction method which developed from this unified theory follows the sequence of the following four basic steps:

1. Prediction of the aerodynamic characteristics (mean velocity, density, and turbulence structure properties)
2. Evaluation of the turbulent-mixing source noise spectrum with the flow properties from step 1 and the Lighthill-Ribner theory (ref. 7)
3. Construction of the far-field sound spectrum at various observer positions from the results of steps 1 and 2, with the source convection and acoustic-mean-flow interaction accounted for through use of Lilley's equation (ref. 6)
4. Computation of the shock-cell noise spectrum from the results of step 1 and the theoretical concepts in reference 13 and addition of these results to the mixing-noise spectra obtained in step 3

### **Jet Plume Aerodynamics**

As discussed above, a prediction of the jet plume aerodynamics is required to provide the strength of the noise sources. The method selected is an extension of Reichardt's theory (ref. 14), which basically synthesizes the complex flows from nozzles of arbitrary geometry by superposition of a suitable distribution of elemental round jet flows.

Reichardt's theory is a semiempirical one, based on extensive experimental observations that the axial momentum flux profiles are bell shaped or Gaussian in the fully developed similarity region (far downstream of the exit plan) of a jet.

From these observations a hypothesis for the relation between axial and transverse momentum flux was formulated, and this hypothesis yields a governing equation for the axial momentum flux. For the similarity region of a circular jet with nozzle area  $A_j$  and exit velocity  $V_j$ , the governing equation and solution are as follows:

$$\frac{\partial}{\partial x} \langle \rho u^2 \rangle = \frac{\lambda(x)}{r} \frac{\partial}{\partial r} \left( r \frac{\partial}{\partial r} \langle \rho u^2 \rangle \right) \quad (1)$$

$$\langle \rho u^2 \rangle = \rho_j V_j^2 \frac{A_j}{\pi b_m^2} \exp[-(r/b_m)^2] \quad (2)$$

where

$$\lambda(x) = \frac{1}{2} b_m \frac{db_m}{dx} \quad (3)$$

$u$  is the axial velocity component,  $\rho$  is density, the angle brackets  $\langle \rangle$  represent the statistical time average, and  $b_m(x)$  is the width of the axial momentum mixing region, taken to be proportional to the axial distance from the nozzle exit plane:

$$b_m(x) = C_m x \quad (4)$$

The jet spreading rate  $C_m$  becomes a key parameter in the theory and is determined experimentally. The coordinate system is shown in figure 1.

Because equation (1) is linear, the summation of elemental solutions (eq. (2)) is also a solution. This unique feature of Reichardt's theory allows the construction of quite complex jet flows with relatively simple mathematics. Although more rigorous (but containing just as much empiricism, albeit in different forms) theories are available for simple jets (circular and planar), there is no other technique available which offers the capability for modeling jet flows typical of aircraft engine suppressor nozzles such as multitube, lobe, and chute nozzles.

Consider a distribution of elemental jets issuing parallel to the  $X$ -axis. The jet exit areas lie in the  $x = 0$  plane. Each elemental jet has an exit area  $A_j = \sigma \, d\sigma \, d\alpha$  located at  $(\sigma, \alpha, 0)$ , as shown in figure 1. The axial momentum flux at a downstream point  $(r, \theta, x)$  due to the elemental jet exhausting at  $(\sigma, \alpha, 0)$  is given by (from eq. (2))

$$d\langle \rho u^2 \rangle = \rho_j V_j^2 (\sigma \, d\sigma \, d\alpha / \pi b_m^2) \exp[-(\xi/b_m)^2] \quad (5)$$

where

$$\xi^2 = r^2 + \sigma^2 - 2r\sigma \cos(\theta - \alpha)$$

Integrating equation (5) results in the following solution:

$$\langle \rho u^2 \rangle(r, \theta, x) = \frac{1}{\pi b_m^2} \iint (\rho_j V_j^2) \exp[-(\xi/b_m)^2] \sigma \, d\sigma \, d\alpha \quad (6)$$

From the distribution of  $\rho_j V_j^2$  in the exit plane, the local value of  $\langle \rho u^2 \rangle$  at any point  $(r, \theta, x)$  can be found from equation (6) by standard numerical integration. If we assume that the jet plume stagnation enthalpy flux  $H$  diffuses in the same manner as axial momentum, an analogous expression for stagnation enthalpy flux  $\langle \rho u H \rangle$  can

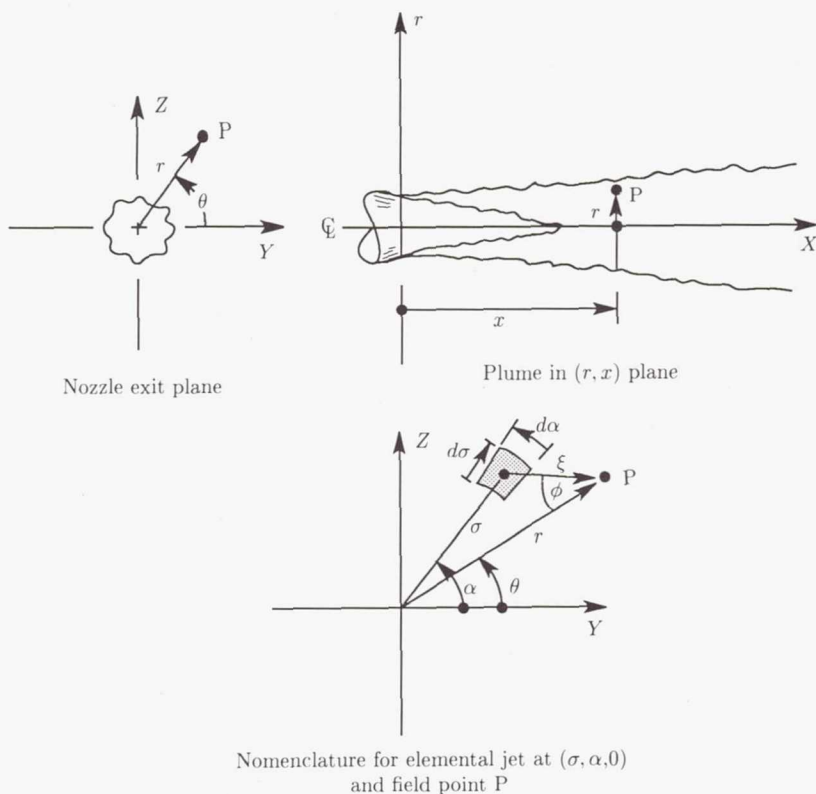


Figure 1. Jet flow coordinate system and nomenclature. (From ref. 10.)

be derived:

$$\langle \rho u H \rangle (r, \theta, x) = \frac{1}{\pi b_h^2} \int \int (\rho_j V_j H_j) \exp[-(\xi/b_h)^2] \sigma \, d\sigma \, d\alpha \quad (7)$$

where  $b_h$  is the width of the thermal shear layer, taken to be proportional to  $x$ :

$$b_h = C_h x \quad (8)$$

for constant  $C_h$ . The stagnation enthalpy is defined as  $H = c_p T_j + (u^2/2) - c_p T_o$  (where  $c_p$  is specific heat at constant pressure,  $T_j$  is jet temperature, and  $T_o$  is ambient temperature), and the thermal layer spreading rate  $C_h$  also must be obtained experimentally. If we assume that the jet mixing occurs at constant static pressure equal to the ambient value, the solutions for  $\langle \rho u^2 \rangle$  and  $\langle \rho u H \rangle$  given by equations (6) and (7) are sufficient to determine the distributions of mean axial velocity  $u$  and temperature  $T_j$  throughout the jet plume.

In addition to the jet plume mean-flow properties, the turbulent Reynolds stress, which is assumed to be proportional to the transverse momentum flux, also can be obtained. Reichardt's hypothesis (from which eq. (1) evolved) states that the transverse momentum flux is proportional to the transverse gradient of the axial

momentum flux, the proportionality factor being  $\lambda(x)$ . For a simple circular jet (eqs. (2) to (4)), the Reynolds stress  $\tau$  is given by

$$\tau = -\langle \rho u'v' \rangle \approx -\lambda \frac{\partial}{\partial r} \langle \rho u^2 \rangle = C_m \rho_j V_j^2 \frac{A_j}{\pi b_m^2} \frac{r}{b_m} \exp[-(r/b_m)^2] \quad (9)$$

where  $u'$  and  $v'$  are the axial and radial components of turbulent fluctuation velocity. For an elemental jet exhausting at  $(\sigma, \alpha, 0)$  the shear stress at  $(r, \theta, x)$  lies along a line connecting  $(\sigma, \alpha, 0)$  and the projection of  $(r, \theta, x)$  onto the  $x = 0$  plane. This vector is at an angle  $\phi$  to the coordinate direction  $r$  (fig. 1). The radial component of the shear stress  $d\tau$  at point  $(r, \theta, x)$  resulting from an elemental jet exhausting at  $(\sigma, \alpha, 0)$  is then  $d\tau_r = d\tau \cos \phi$ . Similarly, the azimuthal component is  $d\tau_\theta = d\tau \sin \phi$ . If we perform the same summation and limiting process over all elemental jets, the total shear stress at  $(r, \theta, x)$  is

$$\tau = (\tau_r^2 + \tau_\theta^2)^{1/2} \quad (10)$$

where

$$\tau_r(r, \theta, x) = \frac{C_m}{\pi b_m^2} \int \int \rho_j V_j^2 (\xi/b_m) \exp[-(\xi/b_m)^2] (\cos \phi) \sigma \, d\sigma \, d\alpha \quad (11)$$

The azimuthal shear stress  $\tau_\theta(r, \theta, x)$  is given by a similar expression with  $\cos \phi$  replaced by  $\sin \phi$ . The distance is again given by the expression from equation (5), and the angle  $\phi$  is given by

$$\xi \cos \phi = r - \sigma \cos(\theta - \alpha) \quad (12)$$

Equations (5) to (12) provide the basic expressions for computation of the jet plume flow parameters  $T_j$ ,  $u$ , and  $\tau$  for a nozzle of arbitrary exit cross section and exit distribution of velocity and temperature. For axisymmetric nozzles,  $\tau = \tau_r$  and  $\tau_\theta = 0$ . The basic limiting assumptions underlying this aerodynamic model for the jet plume characteristics are (1) the jet plume mixing occurs at constant static pressure, equal to the ambient value, and (2) the flow is primarily axial, with all nozzle exit elements in the same plane ( $x = 0$ ).

### Intrinsic Source Intensity Mixing-Noise Spectrum

The aerodynamic characteristics of the jet plume provide the information required to evaluate the acoustic intensity spectrum in the absence of convection and acoustic-mean-flow interaction effects. This represents the sound spectrum which would be heard if the turbulent eddies generating the sound had negligible convection speed relative to the observer and if the velocity and temperature gradients encountered by the sound as it propagated through the jet plume itself had no effect on the sound radiation. As is demonstrated, these effects are indeed powerful for high-velocity jets. The postulation herein is that the basic source strength spectrum can be developed, and the convection and acoustic-mean-flow interaction effects can then be added to this basic (intrinsic) sound spectrum.

The jet plume is first subdivided into elemental "eddy" volumes, each having its own source strength, spectrum, and flow shrouding, as illustrated in figure 2. The

jet noise generation is represented by a collection of convecting and uncorrelated quadrupole sources, each radiating noise with an intensity spectrum directly related to the local flow properties. The net radiation from each eddy is a function of the flow environment of that eddy. Each eddy volume contains a mix of quadrupoles of various orientations. By employing a model of homogeneous, isotropic turbulence in the moving-eddy reference frame and taking the azimuthal average of the resulting sound field, Ribner found that a weighted combination of the various quadrupole types contributes to the net far-field radiation (ref. 7). The amplitude of these quadrupole types is of the form

$$dI(\omega) = \frac{\rho_0 l^3}{c_0^5 R^2} (u')^4 \omega^4 H(\mu) dV \quad (13)$$

where  $dI(\omega)$  is the acoustic intensity per elemental jet volume  $dV$ ,  $\rho_0$  is the ambient density,  $R$  is the source-to-observer distance,  $c_0$  is the ambient speed of sound,  $u'$  is the local turbulence intensity,  $H(\mu)$  is the Fourier transform of the moving-frame space-time cross correlation of  $u'$ , and  $\mu$  is the ratio of emitted frequency  $\omega$  to characteristic frequency  $\omega_0$ . Equation (13) is used to calculate the mixing-noise amplitude and frequency content for each volume element in the jet. The characteristic turbulence frequency and length scale for each eddy volume are determined from the local mean-flow velocity, temperature, and shear stress with the empirically derived similarity relations of reference 15:

$$\left. \begin{aligned} \omega_0 &\approx \partial U / \partial r \\ l &\approx u' / \omega_0 \end{aligned} \right\} \quad (14)$$

where  $l$  is the characteristic turbulent eddy size and the turbulence intensity is obtained from the shear stress as follows:

$$u' \approx \sqrt{\tau / \rho}$$

### Acoustic-Mean-Flow Interaction Model

The equation which describes the propagation of sound emitted by the turbulence in a jet was developed in reference 6 and is as follows:

$$\frac{1}{c^2} D_*^3 p - D_*(\Delta p) \frac{d}{dr} (\log c^2) D_* \left( \frac{\partial p}{\partial r} \right) + 2 \frac{\partial u}{\partial r} \frac{\partial^2 p}{\partial \times \partial r} = S \quad (15)$$

where

$$D_* = \frac{\partial}{\partial t} + U \frac{\partial}{\partial x} \quad \text{and} \quad S = \rho D_* [\nabla \cdot \nabla \cdot (u' \cdot u')] \quad (16)$$

In equations (15) and (16),  $U = U(r)$ ,  $c = c(r)$ , and  $\rho = \rho(r)$  are the azimuthally averaged mean-flow axial jet velocity, speed of sound, and density, respectively. The symbol  $\Delta$  is the Laplacian operator,  $t$  is time, and  $u'$  is essentially the turbulent velocity fluctuation. Roughly speaking,  $S$  is the noise source strength which drives

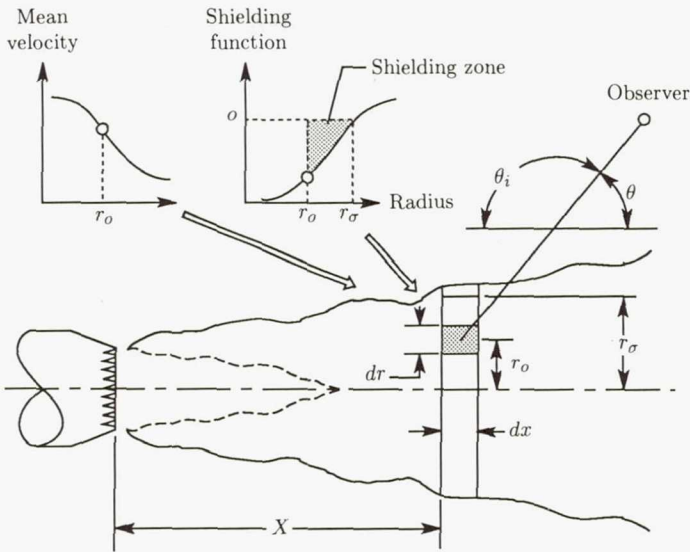


Figure 2. Generalized volume element model. (From ref. 12.)

the acoustic pressure fluctuations  $p$ . Equation (15) is a third-order wave equation for the variable  $p$ , and this equation explicitly displays the influence of mean velocity  $U(r)$  and temperature (through speed of sound  $c(r)$ ) profiles on the propagation of noise.

To solve equation (15), the profiles for  $U(r)$ ,  $c(r)$ ,  $\rho(r)$ , and  $S(r)$  must first be prescribed. These are provided by the aerodynamics calculation described in the previous section. The Green's function solution for equation (15), when convoluted with the source term  $S$ , provides the solution to Lilley's equation. From the Green's function, solutions for higher order singularities (dipoles and quadrupoles) can be obtained by differentiating the source solution with respect to source coordinates. The right-hand side of equation (15),  $S(r)$ , represents a mix of quadrupoles of various orientations, as discussed in the previous section. The various quadrupole contributions are added in the manner developed in reference 7, but with each quadrupole type having its own solution form representing the combined effects of convection and acoustic-mean-flow interaction.

The combined convection and interaction effects can be thought of as a multiplier of the basic source intensity spectrum given by equation (13), and this multiplier is a function of the local mean-flow properties and their radial gradients. It includes the effects of the following:

1. Convection—the effect of source motion relative to the observer, sometimes called the Doppler effect
2. Refraction—the alteration of the sound pressure and directivity as it propagates through a moving fluid with cross-stream gradients
3. Shielding—the decay of the sound as it propagates through portions of the mean-flow gradients where wave-like behavior gives way to exponential decay

Details of the acoustic-mean-flow interaction theoretical development can be found in reference 5. The details of the aerodynamic theory and source intensity spectrum model development can be found in references 9 and 14. The analytical model does take into account Mach wave radiation associated with eddies convecting at supersonic speeds (which, in turn, tends to amplify the noise levels in the region near the jet axis).

The above analytical model elements have been integrated into a unified computational procedure. The jet plume is subdivided into elemental eddy volumes (as previously mentioned), each having its own source strength, spectrum, and flow shrouding, as illustrated in figure 2. The simple closed-form acoustic pressure solutions, combined with the simple aerodynamics calculation method, permit rapid, economical computations of the entire jet plume aerodynamic and acoustic characteristics, including far-field spectra at all observer angles. The contributions from each elemental jet volume, in each frequency band, are simply added based on mean-square pressure. The shock-cell noise contribution is then computed separately and added to the mixing-noise contribution to yield the total far-field spectra.

### **Comparisons of Model Predictions With Experiment**

Many comparisons of the predicted and measured far-field acoustic spectra of nozzles of various types have been carried out, and these results are reported in references 9 to 12. Typical examples of sound pressure level (SPL) spectra for a single-stream conical nozzle and overall sound pressure level (OASPL) for a dual-flow conventional bypass nozzle are shown in figures 3 and 4, respectively. These comparisons of prediction with experiment show that the unified aeroacoustic jet noise prediction model described above duplicates the characteristic behavior of these simple nozzles rather well. In particular, the spectrum shapes agree quite well and the trends of OASPL as a function of velocity ratio  $V_o/V_i$  and area ratio  $A_o/A_i$  predicted by the theory are consistent with the experimental results. Note that the magnitude and location of the noise minimum as a function of velocity ratio shown in figure 4 for the dual-flow coaxial jet is predicted quite well.

Comparisons of predicted noise characteristics with measured characteristics for an inverted-flow coannular nozzle are shown in figures 5 and 6 (taken from ref. 11). Note that the observed "double-peak" spectrum shape is predicted fairly well by the theory. Comparisons of predicted noise trends with measured trends for a 36-element multichute nozzle are shown in figures 7 and 8 (taken from ref. 12). The characteristic flat spectrum shape is well modeled, and the trend of noise dependence on chute area ratio (defined as annulus area divided by flow area) and jet velocity is also well predicted.

The comparison results shown in figures 3 to 8 provide reasonable verification that the unified theoretical model for predicting jet noise described herein has the necessary ingredients (i.e., the important physical mechanisms) for analyzing and diagnosing the mechanisms for controlling jet noise.

### **Noise Suppression Mechanisms**

#### *Conventional Bypass Versus Inverted-Flow Nozzles*

Based on the reasonable successes achieved in predicting the aeroacoustic characteristics of a wide variety of nozzle types over a range of operating conditions (as

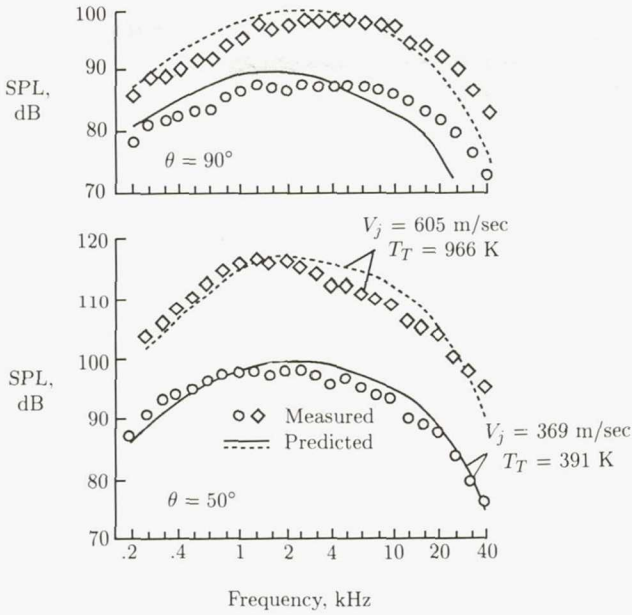


Figure 3. Conical nozzle predicted and measured SPL spectra. (From ref. 11.)

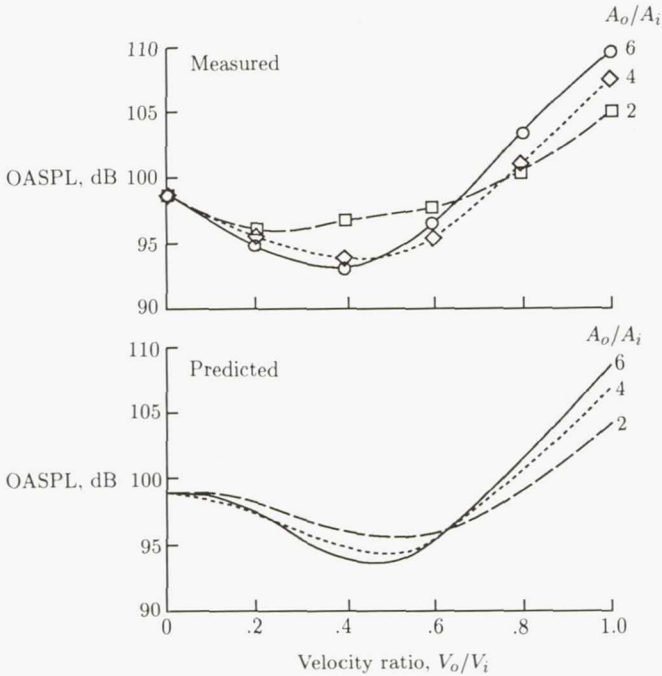


Figure 4. Influence of area ratio on conventional bypass jet OASPL.  $\theta = 90^\circ$ ;  $V_i = 305$  m/sec;  $T_{t,i} = 700$  K;  $T_{T,o} = 300$  K. (From ref. 11.)

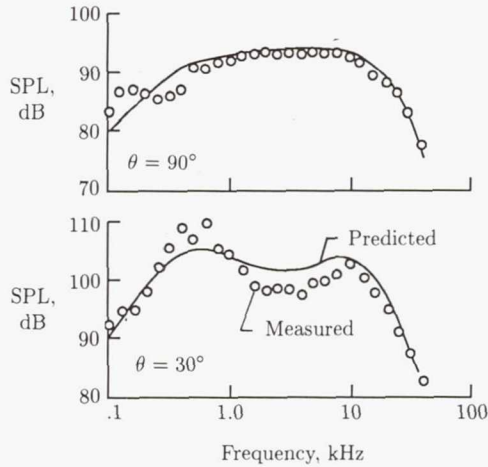


Figure 5. Measured and predicted SPL spectra for inverted-flow coannular nozzle with  $A_o/A_i = 0.4$ ;  $V_o/V_i = 1.5$ ;  $V_i = 366$  m/sec;  $V_o = 549$  m/sec;  $T_{T,i} = 556$  K;  $T_{T,o} = 667$  K;  $R = 12.2$  m;  $D_i = 11.8$  cm. (From ref. 11.)

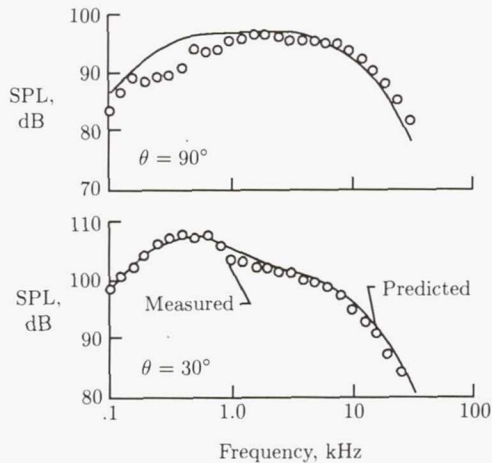


Figure 6. Measured and predicted SPL spectra for inverted-flow coannular nozzle with  $A_o/A_i = 2.0$ ;  $V_o/V_i = 1.5$ ;  $V_i = 305$  m/sec;  $V_o = 457$  m/sec;  $T_{T,i} = 294$  K;  $T_{T,o} = 556$  K;  $R = 12.2$  m;  $D_i = 11.8$  cm. (From ref. 11.)

summarized in the preceding section and detailed in refs. 9 to 12), it was deemed worthwhile to utilize the theory to analyze the noise suppression mechanisms of coannular nozzles. Of particular interest was how flow inversion (i.e., ducting the high-velocity hot stream to the outside) could provide noise reduction for dual-flow exhaust systems. Theoretical predictions were made of a conventional bypass and an inverted-flow coannular nozzle. The nozzles were sized to give the same thrust and equal primary (high-velocity) and secondary (low-velocity) flow areas. The two nozzles therefore had equivalent thrust, mass flow, primary and secondary stream

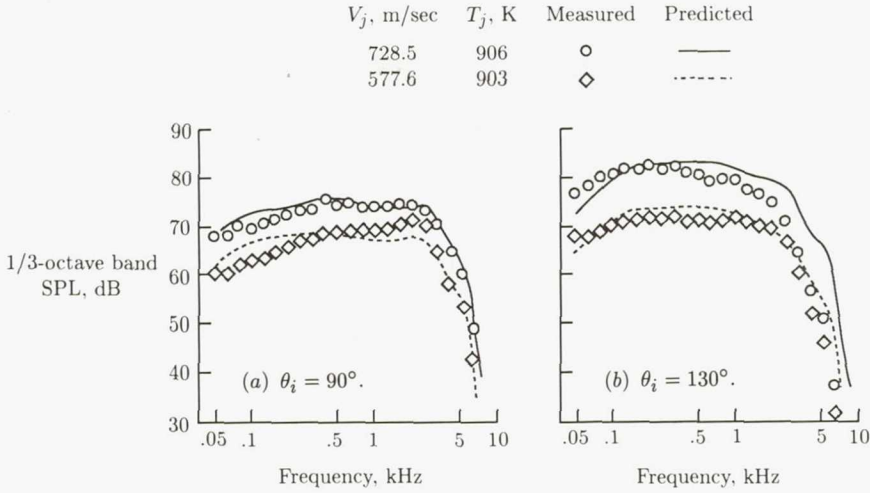


Figure 7. Predicted and measured SPL spectra for 36-chute turbojet suppressor nozzle with area ratio of 2.0. (From ref. 12.)

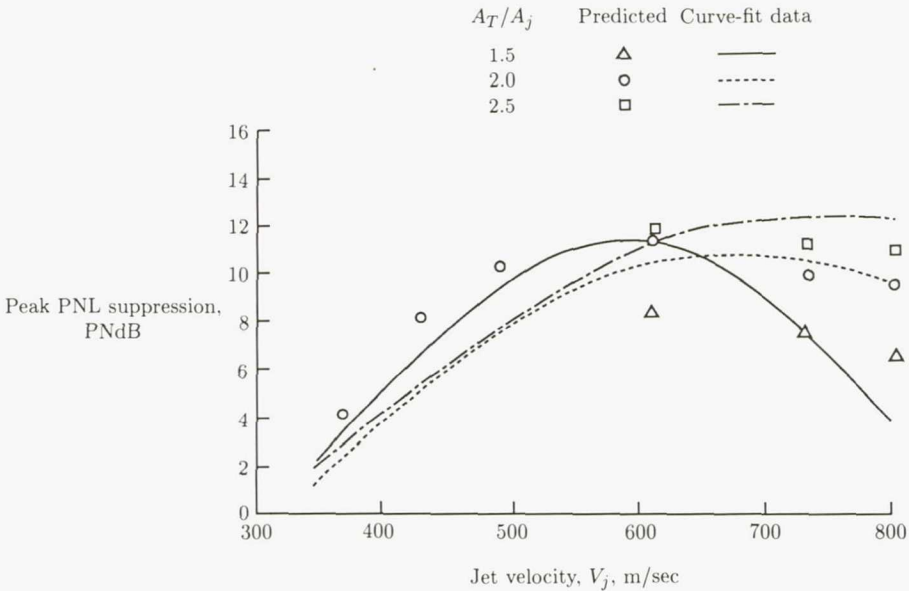


Figure 8. Predicted and measured effect of area ratio on peak PNL suppression for 36-chute turbojet suppressor nozzle. (From ref. 12.)

velocities, and temperatures; thus, the differences in noise should have been solely a function of jet plume profile development and mixing.

Aeroacoustic predictions were made for both a conventional bypass and an inverted-flow nozzle for velocity ratio  $V_s/V_p = 0.7$  and area ratio  $A_s/A_p = 1.0$ , where subscripts  $p$  and  $s$  refer to primary and secondary streams. Figure 9 shows mean

axial velocity  $U$  profiles across the jet plume at several axial stations  $x/D_p$  along the plume. The normalized peak velocity at any axial station  $U_p$  versus downstream distance is presented in figure 10 for the two nozzle types. These results show that the flow inversion produces more rapid plume decay. Figure 11 shows axial turbulence velocity, a key ingredient in the mixing-noise source strength, at several axial stations along the plume. This figure shows the expected lower turbulence levels at small values of  $x/D_p$  for the conventional bypass jet and higher levels of turbulence at large  $x/D_p$  than the inverted-flow nozzle.

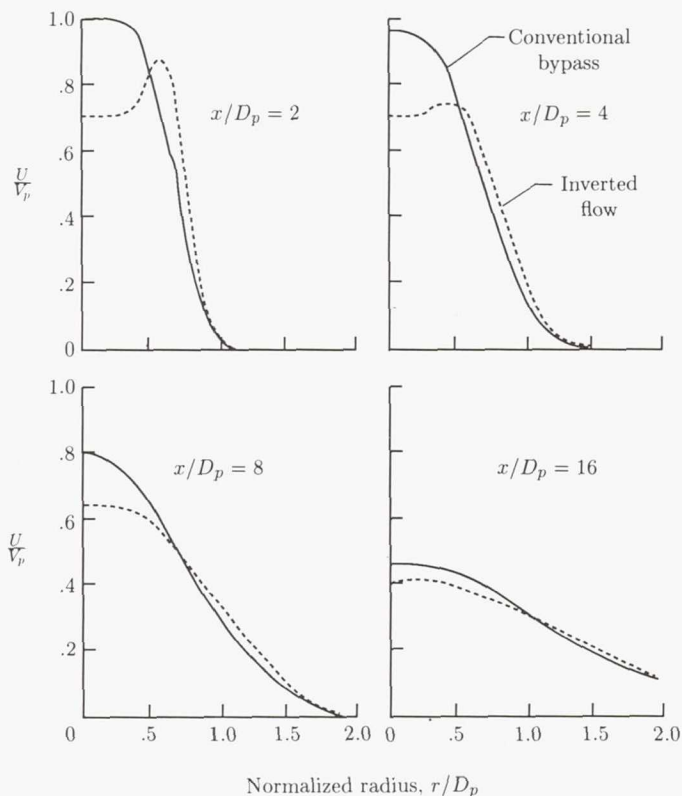


Figure 9. Inverted-flow and conventional bypass mixing mean velocity profiles.  
(From ref. 11.)

The corresponding far-field acoustic spectra are shown in figure 12. At  $\theta = 90^\circ$  (i.e., in the plane of the nozzle exit), the inverted-flow nozzle exhibits higher noise at high frequencies and lower noise at low frequencies than the conventional bypass nozzle. Since the high-frequency noise generally comes from regions close to the nozzle exit, the highest high-frequency noise correlates with the highest turbulence levels at small values of  $x/D_p$  shown in figure 11. Similarly, low-frequency noise is primarily from the fully developed regions far downstream, and the lowest low-frequency noise of the inverted-flow nozzle correlates with its lowest turbulence levels for large  $x/D_p$ .

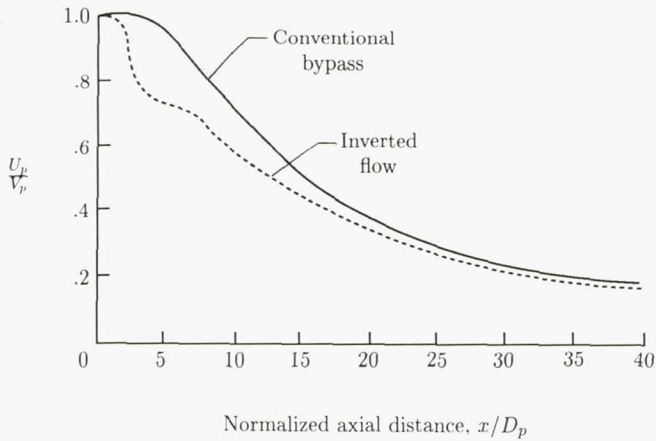


Figure 10. Inverted-flow and conventional bypass mixing peak velocity axial decay. (From ref. 11.)

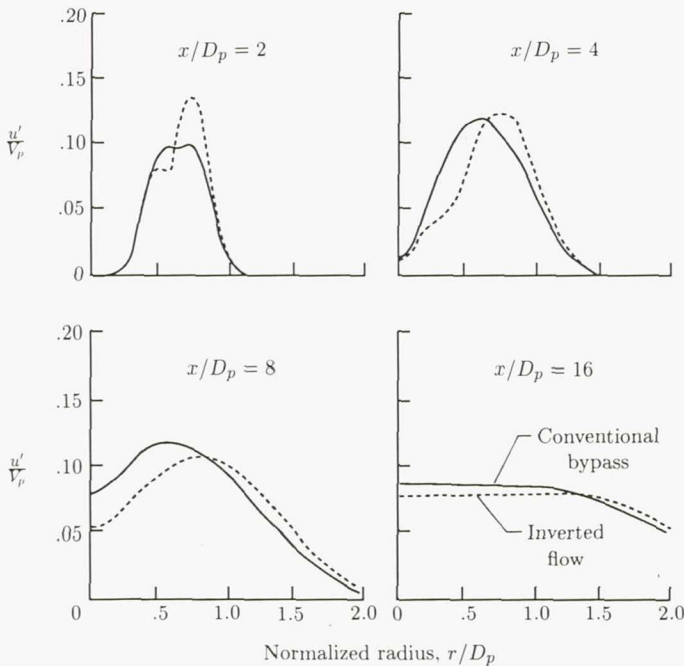


Figure 11. Inverted-flow and conventional bypass mixing turbulence intensity profiles. (From ref. 11.)

The results in figure 12 for  $\theta = 50^\circ$  ( $130^\circ$  from the inlet axis), however, show the inverted-flow jet noise to be lower than that of the conventional bypass nozzle throughout the spectrum. This lower noise is primarily a result of reduced convective amplification, that is, lower eddy convection speeds. The eddy convection speed is proportional to the peak mean axial velocity, and the peak velocity curves shown in figure 10 imply that the inverted-flow jet exhibits lower convection speeds, and

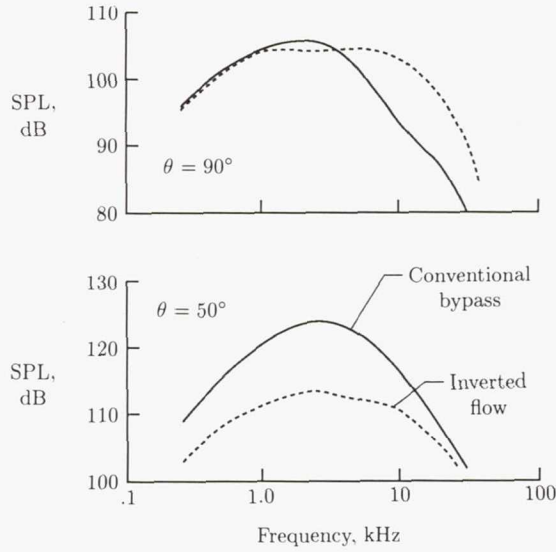


Figure 12. Inverted-flow and conventional bypass mixing SPL spectra. (From ref. 11.)

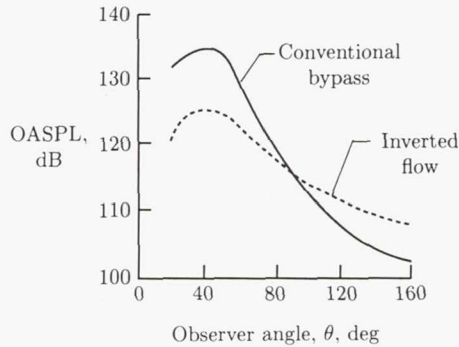


Figure 13. Inverted-flow and conventional bypass mixing OASPL directivity. (From ref. 11.)

therefore reduced convective amplification, than the conventional bypass nozzle. Figure 13 shows nozzle overall sound pressure level (OASPL) versus angle for the two nozzles. Note the shallower slope of the directivity curve for the inverted-flow nozzle, a result of reduced convective amplification.

To demonstrate the influence of flow shielding as a noise reduction mechanism, the above predictions were repeated with the shielding effects in the acoustic-mean-flow interaction model suppressed. These results are shown in figure 14 for  $\theta = 30^\circ$ . First of all, flow shielding effect is less for the inverted-flow nozzle than for the conventional bypass nozzle, but the reduced convective amplification more than compensates for the loss. The main point to observe is that the shielding effect is substantial at angles

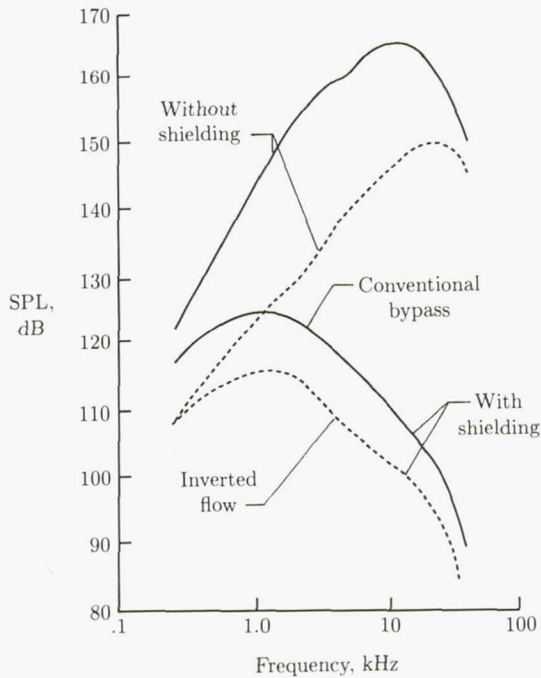


Figure 14. Influence of flow shielding on inverted-flow and conventional bypass nozzle SPL spectrum.  $\theta = 30^\circ$ . (From ref. 11.)

close to the jet axis, being on the order of 30 to 40 dB at  $\theta = 30^\circ$  for these cases. The shielding effect also increases with increasing frequency, as figure 14 shows.

#### Multielement Nozzles

The theoretical concepts for jet noise generation and radiation discussed in the previous sections can be evaluated through use of the analytical model in selective modes. The objective is to identify the relative roles these mechanisms play in the generation and suppression of jet noise. Such a study was carried out with a multielement, 36-chute suppressor nozzle used as a representative case study (ref. 12). The basic jet noise mechanisms are as follows:

1. Turbulent-mixing-noise generation
2. Convective amplification
3. Fluid shielding
4. Shock-cell noise

It is of interest to evaluate how the individual mechanisms combine to yield the far-field result and, more importantly, how these mechanisms change due to the addition of a suppressor to a baseline nozzle.

A parametric study was performed to evaluate the relative contributions of the four mechanisms to the far-field noise for both a baseline conical nozzle and a typical high-suppression, multielement nozzle. A 36-chute turbojet suppressor with a ratio of total nozzle area  $A_T$  to flow area  $A_j$  of 2.0 was chosen for this study as representative

of a high-element-number, high-suppression (10 to 12 PNdB) exhaust system. A typical takeoff condition of  $V_j = 732$  m/sec (2400 ft/sec) and  $T_j = 906$  K (1630°R) was selected for evaluation. The exit area of both the baseline conical nozzle and the 36-chute suppressor nozzle was  $0.218$  m<sup>2</sup> (338 in<sup>2</sup>). Noise characteristics were predicted for a 732-m (2400-ft) sideline distance.

The prediction computations were performed in the following four modes: (1) complete acoustic calculation; (2) as in (1), but with shock-cell noise omitted; (3) as in (2), but with fluid shielding omitted; and (4) as in (3), but with convective amplification omitted. (For the 36-chute suppressor, mode (1) was omitted since the ability to model shock-cell noise of multichute nozzles was not established at the time these computations were performed. However, Stone has evolved a semiempirical prediction method for shock-cell noise of multielement suppressor nozzles utilizing more recent data. (See ref. 16 for more details.) The difference in noise levels between modes (1) and (2) is a measure of the shock-cell noise contribution to the total jet noise signature. The difference in noise levels between modes (2) and (3) is a measure of the influence of fluid shielding on the jet noise. Finally, the difference in noise levels between modes (3) and (4) indicates the amount of convective amplification that is present in the jet.

The results of the above series of computations are summarized in figures 15 to 17. Figure 15 shows the perceived noise level (PNL) directivity patterns for the different prediction modes. Also shown for comparison are measured data from reference 12, which should be compared with mode (1) predictions (mode (2) for the 36-chute nozzle). Figures 16 and 17 show the corresponding spectrum shapes (1/3-octave SPL) at 50° and 130° relative to the inlet axis. The measured spectra are also shown for reference.

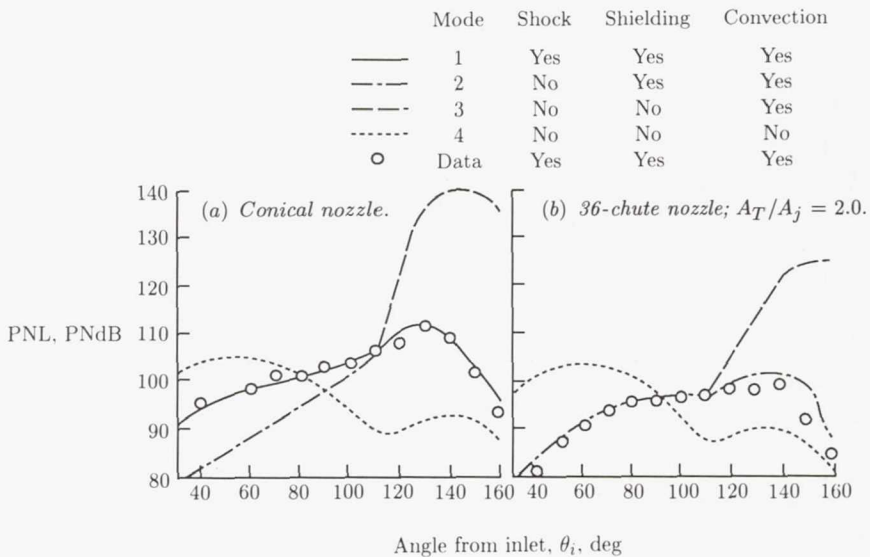


Figure 15. Relative contribution of noise mechanisms to PNL directivity at  $V_j = 732$  m/sec. (From ref. 12.)

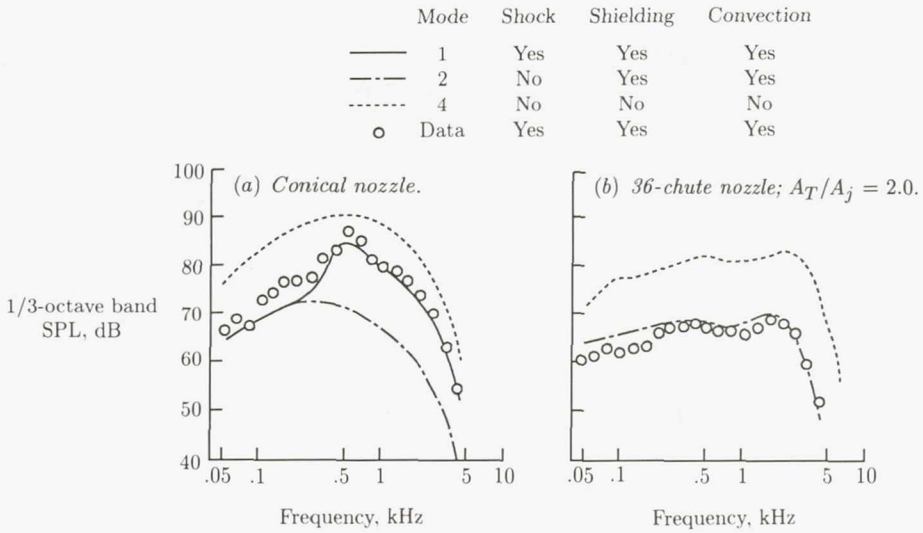


Figure 16. Relative contribution of noise mechanisms to SPL spectra at  $\theta_i = 50^\circ$  for conical nozzle and 36-chute nozzle at  $V_j = 732$  m/sec. (From ref. 12.)

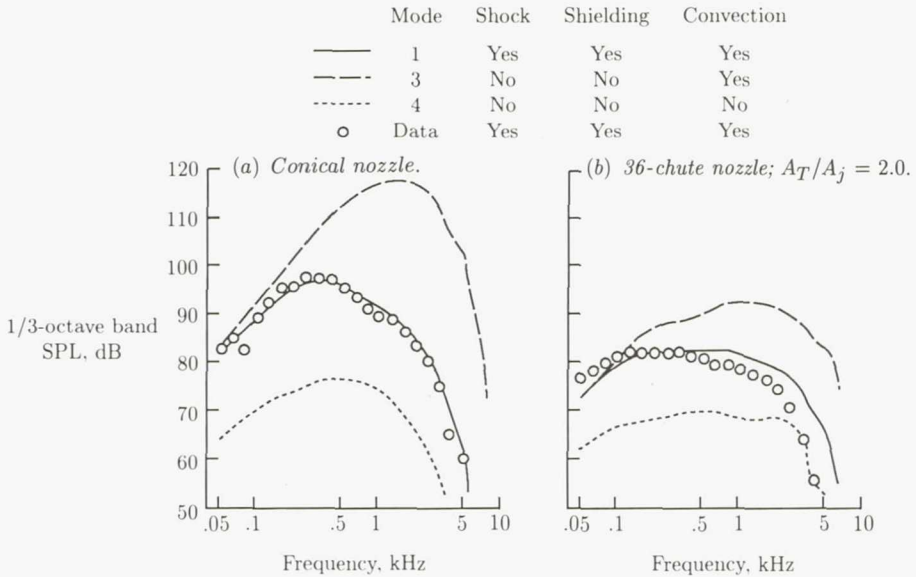


Figure 17. Relative contribution of noise mechanisms to SPL spectra at  $\theta_i = 130^\circ$  for conical nozzle and 36-chute nozzle at  $V_j = 732$  m/sec. (From ref. 12.)

For the conical nozzle PNL directivity patterns (fig. 15), the shock-cell noise contributes substantially to the total noise in the forward quadrant, that is, at angles to the inlet less than  $90^\circ$ . This contribution can be seen in the difference between

mode (1) and (2) predictions. There is no contribution of shock-cell noise close to the jet axis (i.e., at angles greater than  $120^\circ$  from the inlet axis), since predictions for modes (1) and (2) are the same in this region. There is no fluid shielding for observer angles less than about  $110^\circ$ , based on a comparison of predictions for modes (2) and (3). For angles greater than  $110^\circ$ , however, shielding effects become quite substantial, on the order of 30 PNdB. Eddy-convection effects are also large; they increase the noise in the aft quadrant (angles greater than  $90^\circ$ ). This effect is apparent from comparing predictions for modes (3) and (4).

The prediction for mode (4) shown in figure 15(a) represents the basic turbulent-mixing noise in the absence of convection and fluid-shielding effects. It possesses a basic, nonconstant directivity pattern dictated by the weighted summation of various quadrupole types composing the turbulent eddies. This basic pattern is only symmetric about  $90^\circ$  when the local flow Mach number is zero because the quadrupole weighting factors are a function of local Mach number and bias the radiation toward the forward quadrant.

The corresponding PNL directivity patterns for the 36-chute suppressor are shown in figure 15(b). The trends discussed above for the conical nozzle are qualitatively similar for the 36-chute nozzle, with the exception of the shock-cell noise contribution. The predictions were made with the shock-cell noise neglected (mode (2)), and yet the predictions agree well with the data, as figure 15(b) shows. This finding implies that shock-cell noise is not a significant feature of a high-element-number multichute nozzle. It also appears that neither convection effects nor fluid-shielding effects are as strong as for the conical nozzle.

The breakdown of mechanisms for a typical forward-quadrant angle of  $50^\circ$  is shown in figure 16. No shielding occurs at this angle; therefore, the mode (3) results are omitted, as they are identical to the mode (2) results. The conical-nozzle results (fig. 16(a)) show an interesting counteraction among the mechanisms. The basic mixing-noise spectrum (mode (4)) yields a high noise level, much higher than the measured level. The convection effect is to Doppler shift and drop this spectrum to a level significantly lower than the data (except at very low frequencies), as indicated by the mode (2) prediction. Finally, the addition of the shock-cell noise spectrum raises the spectrum back to the measured level at middle to high frequencies.

The corresponding spectrum results for the 36-chute nozzle are shown in figure 16(b). The good agreement between the spectrum prediction and the measured spectrum for mode (2) substantiates the implication from figure 15(b): shock-cell noise may not be a significant source for a high-element-number multichute suppressor. However, acoustic data for multielement suppressors employing fewer elements (e.g., 20) show evidence of shock-cell noise in the forward quadrant, particularly in flight. (See ref. 16.) Again, the effect of convection is to reduce the level and Doppler shift the spectrum to lower frequencies.

Near the peak noise angle of  $130^\circ$ , convection effects are significant. They produce a dramatic amplification of the mixing noise, as the results in figure 17 show. Another counteraction of mechanisms occurs at this angle and involves the competing effects of convection and fluid shielding. The basic mixing-noise spectrum (mode (4)) is much lower than the measured level, as shown in figure 17(a). The effect of convection is to increase the levels by as much as 40 to 50 dB at high frequencies. The effect of shielding, however, is to reduce the noise levels by 20 to 30 dB at high frequencies, consistent with the measured levels.

It is interesting to note that the convection effect Doppler shifts the basic mixing-noise spectrum to higher frequencies, as would be expected from classic notations of moving-source acoustics. However, the fluid-shielding effects, which increase with increasing frequency, attenuate the high-frequency portion of the convected spectrum to such a large extent that the resulting spectrum peaks at a much lower frequency, lower than even the basic unconvected spectrum peaks. This attenuation explains the observed "reverse Doppler shift" at angles close to the jet axis.

The competing influences of convection and fluid shielding are also evident in the predictions for the 36-chute nozzle shown in figure 17(b). The magnitudes of these effects are considerably smaller than those exhibited by the conical nozzle. For example, at 2000 Hz the convective amplification is 22 dB for the 36-chute nozzle, compared with 48 dB for the conical nozzle at the same frequency. Similarly, the fluid-shielding attenuation is only 12 dB at 2000 Hz for the chute nozzle, compared with 31 dB of attenuation for the conical nozzle.

The various suppression mechanisms can be isolated explicitly by examining the difference between the various prediction curves shown in figures 15 to 17. First, the total PNL suppression as a function of angle is the difference between the conical- and 36-chute-nozzle total noise PNL directivity patterns. This difference can be compared with measured PNL suppression and is shown in figure 18. The predicted total PNL suppression compares well with the measured suppression.

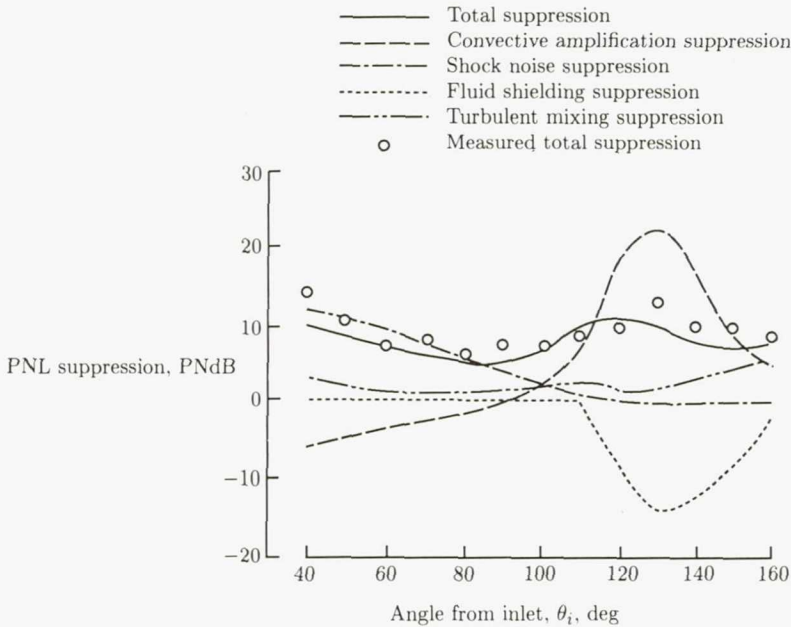


Figure 18. PNL suppression composition for 36-chute nozzle at  $V_j = 732$  m/sec.  $A_T/A_j = 2.0$ . (From ref. 12.)

For the results of figures 15 to 17, it can be concluded that the high-element-number multichute nozzle almost completely suppresses the shock-cell noise and thus permits the mixing noise to dominate the forward-quadrant spectra. The shock-cell noise suppression is then approximated by the difference between mode (1) and

mode (2) conical-nozzle predictions. This estimated shock-cell noise suppression is higher than the total predicted suppression in the forward quadrant; hence, some other mechanism is providing negative suppression, that is, increasing the PNL.

The suppression due to convective amplification can be computed by first calculating the convective amplification for each nozzle (mode (3) PNL minus mode (4)) and then subtracting the 36-chute-nozzle result from the conical-nozzle result. The convective amplification suppression is shown in figure 18. Note that it is negative in the forward quadrant; this explains why the shock-cell noise suppression is greater than the total (net) suppression.

Similarly, the difference between the fluid-shielding attenuation for the 36-chute suppressor and the conical nozzle was computed from the results shown in figure 15, and this difference is also shown in figure 18. From this result, it is apparent that a multielement suppressor exhibits less fluid-shielding effects than a conical nozzle, that is, part of the beneficial effect of fluid shielding is lost by the addition of a suppressor.

The observed suppression in the aft quadrant is primarily a result of reduced convective amplification, offset somewhat by a loss in fluid shielding. This delicate balance between convection and shielding effects in the aft quadrant is very difficult to predict accurately because these two effects are large in magnitude but opposite in sign, as illustrated in figure 17.

Finally, the suppression of basic turbulent-mixing-noise generation has been evaluated by subtracting the prediction for mode (4) for the 36-chute nozzle from that for the conical nozzle, and this result is also shown in figure 18. The basic mixing-noise suppression is quite small, from 1 to 5 dB over the range of angles shown, and this result is contrary to historical conceptions of how much multielement suppressors suppress jet noise.

The multichute suppressor in fact generates approximately the same total mixing noise as the equivalent conical nozzle but redistributes the noise to higher frequencies. This is dramatically illustrated in figure 19, in which the basic mixing-noise spectra (mode (4)) for the two nozzles are presented. Also shown are these same spectra with the atmospheric air attenuation removed (i.e., the "lossless" spectra). The multichute lossless spectrum has about the same peak level as the conical-nozzle lossless spectrum, but at a much higher frequency. The ratio of 36-chute-nozzle peak-noise (lossless) frequency to conical-nozzle peak-noise (lossless) frequency is about 6:1. This is precisely the ratio of the conical-nozzle diameter to 36-chute-nozzle equivalent-area diameter.

The reduction in shock-cell noise produced by a multichute suppressor can be explained by the fact that breaking up a large, round jet into very small, discrete, rectangular jets will cause the shock-cell formation to be dissipated much more rapidly. The shock-cell spacings and cross-sectional dimensions will be much smaller, and the cells are likely to be less numerous. The resulting radiation is therefore likely to be much lower in level and higher in frequency than that for a conical nozzle.

The observation that the total generated mixing noise is not significantly different for a multichute suppressor than for a conical nozzle is explained by the fact that the multichute-nozzle mixing layer perimeter close to the nozzle exit plane is considerably larger than that of an equivalent-area conical nozzle. The high-frequency noise generated in the initial shear layers should therefore be higher by the

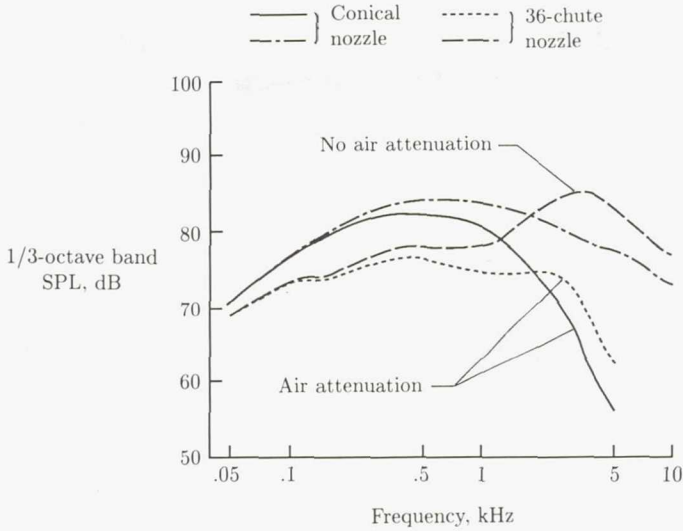


Figure 19. Predicted turbulent-mixing-noise spectra at  $\theta_i = 90^\circ$  for conical nozzle and 36-chute nozzle ( $A_T/A_j = 2.0$ ) at  $V_j = 732$  m/sec. (From ref. 12.)

ratio of perimeters, provided the premerged portions of the chute mixing layers have approximately the same turbulence characteristics. Once the chutes have merged, a large, axisymmetric jet forms which has a substantially lower velocity than the exit value; therefore, the multichute-nozzle low-frequency noise levels should be lower than the corresponding conical-nozzle levels.

The reduction in convection effects exhibited by a multichute nozzle is the result of lower eddy-convection velocities. The rapid decay of plume mean velocity exhibited by a multichute nozzle suggests that the majority of the noise-producing turbulent eddies in the plume are convecting downstream at a substantially lower velocity than in a conical nozzle.

The reduced fluid-shielding effects characteristic of a multichute nozzle can also be related to the rapid plume velocity (and temperature) decay. Fluid shielding increases with increasing plume flow velocity and temperature; therefore, the lower velocity and temperature levels resulting from the rapid chute-element mixing provide less fluid shielding than those of an equivalent-area conical nozzle.

From the preceding considerations, it can be concluded that the best suppression is achieved by producing the most rapid plume decay. Higher numbers of elements and higher area ratios give more rapid decay. Area ratio seems to control the velocity level plateau formed by the merging of the individual chute element jets into a single annular jet. Higher area ratios yield lower merged-velocity levels and hence lower convection speeds. Element number seems to control how fast the merged-velocity level is reached; higher numbers of elements give more rapid decay of the individual element jet flows to the merged-velocity level. One additional benefit of higher numbers of elements is that the initial mixing-noise generation is pushed to higher frequencies by virtue of the smaller turbulence scales associated with the smaller, individual jet elements.

## **Jet Noise Suppression Concepts**

Various experimental studies have demonstrated the noise reduction potential of jet noise suppression concepts which essentially alter the jet plume development. All these concepts may be grouped under the following two broad categories:

1. Geometric concepts, such as multielement suppressors (e.g., chutes, spokes, and tubes) at the nozzle exit plane, ejectors surrounding the jet in the vicinity of the nozzle exit, annular plug or 2-D nozzles, and combinations of the above.

2. Aerothermodynamic concepts, such as inverted-velocity profile (i.e., a higher velocity jet surrounding a lower velocity jet), thermal acoustic shield (i.e., surrounding either fully or partially the main jet with a jet having a high static temperature and low velocity), and shock noise control by appropriate contouring of the nozzle flow path.

Some jet noise suppression concepts have employed a combination of both geometric and aerothermodynamic concepts (e.g., a dual-flow, multielement suppressor with inverted-velocity profile).

This section presents the experimental data for the above two categories collected over several years, explains the data based on physical reasoning, and evolves guidelines (where possible) for future design of jet noise suppression devices.

### **Geometric Concepts**

#### *Multielement Suppressors*

The principal jet noise suppression mechanism underlying the multielement suppressors (such as chutes, spokes, or tubes) is the division of the large single jet into many small jets with sufficient separation between these jets to enhance mixing with the ambient air to yield a rapid decay of the jet plume. Mixing is enhanced by the increased surface area of the jet available for shear with the ambient air, a classic momentum diffusion concept. Also, since each small jet has a much smaller equivalent diameter than a circular jet, its effectiveness as a noise radiator is restricted to a much smaller physical length compared with the single large jet, as long as the separate jets do not merge. The merged jet will have a much lower jet velocity. This lower velocity results in the acoustic energy being transferred to smaller scale turbulent eddies which, by virtue of their small size, generate noise in the higher frequency ranges than the turbulent eddies of a large single jet. This higher frequency noise generation results in a suppressor spectrum which has high- and low-frequency peaks, unlike the conical nozzle, which has a low-frequency peak only. (See fig. 20, from ref. 17.) The acoustic signal suffers atmospheric absorption in reaching the far-field observer. As various data and theories have indicated (refs. 18 and 19), high-frequency acoustic waves suffer significantly more atmospheric attenuation than low-frequency waves over the same distance. Since multielement suppressors have a larger contribution of acoustic energy in the high-frequency region and that energy suffers much higher levels of atmospheric absorption, the far-field noise of these suppressors is lower than that of single conical nozzles.

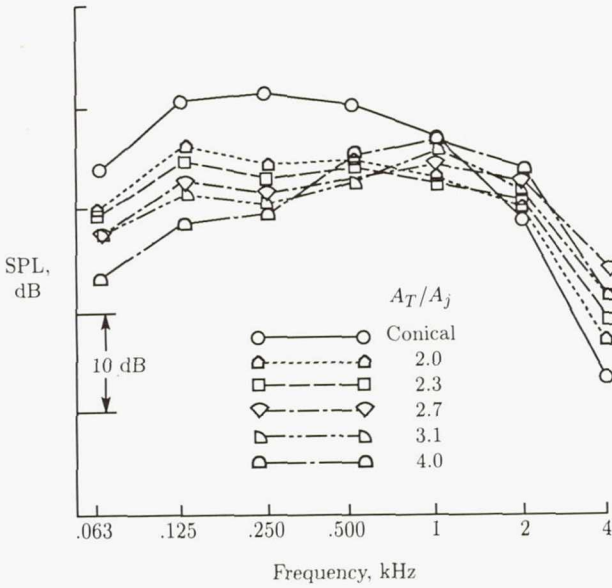


Figure 20. Spectra illustrating dual-peak characteristics of multitube nozzles.  $NPR \approx 2.1$ ;  $T_T \approx 1520^\circ R$ ;  $V_j \approx 1870$  ft/sec. (From ref. 17.)

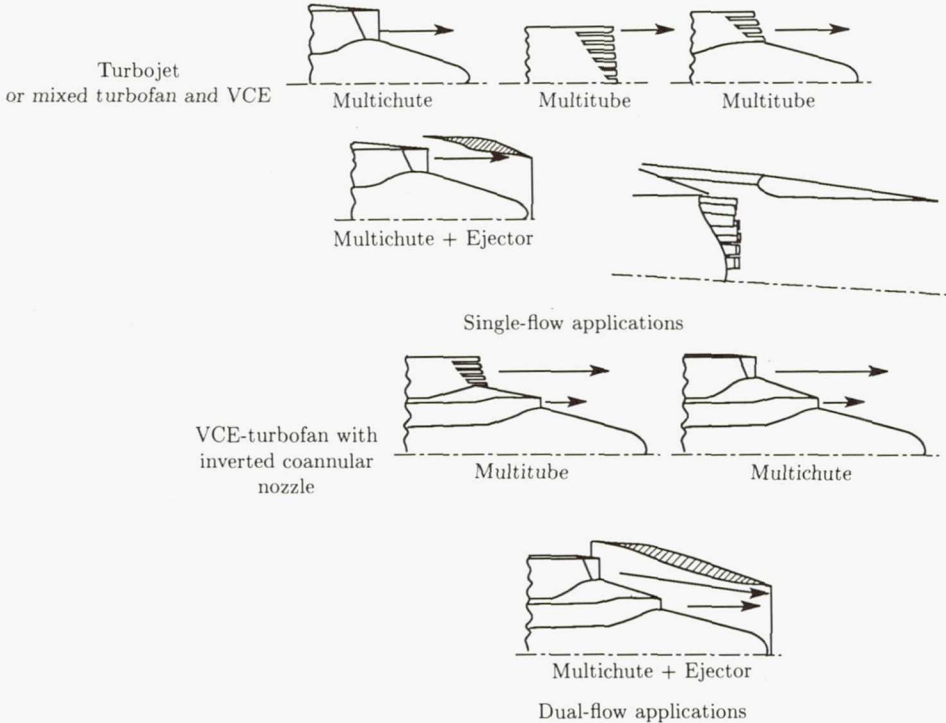


Figure 21. Examples of multi-element suppressors with and without ejectors. (From ref. 20.)

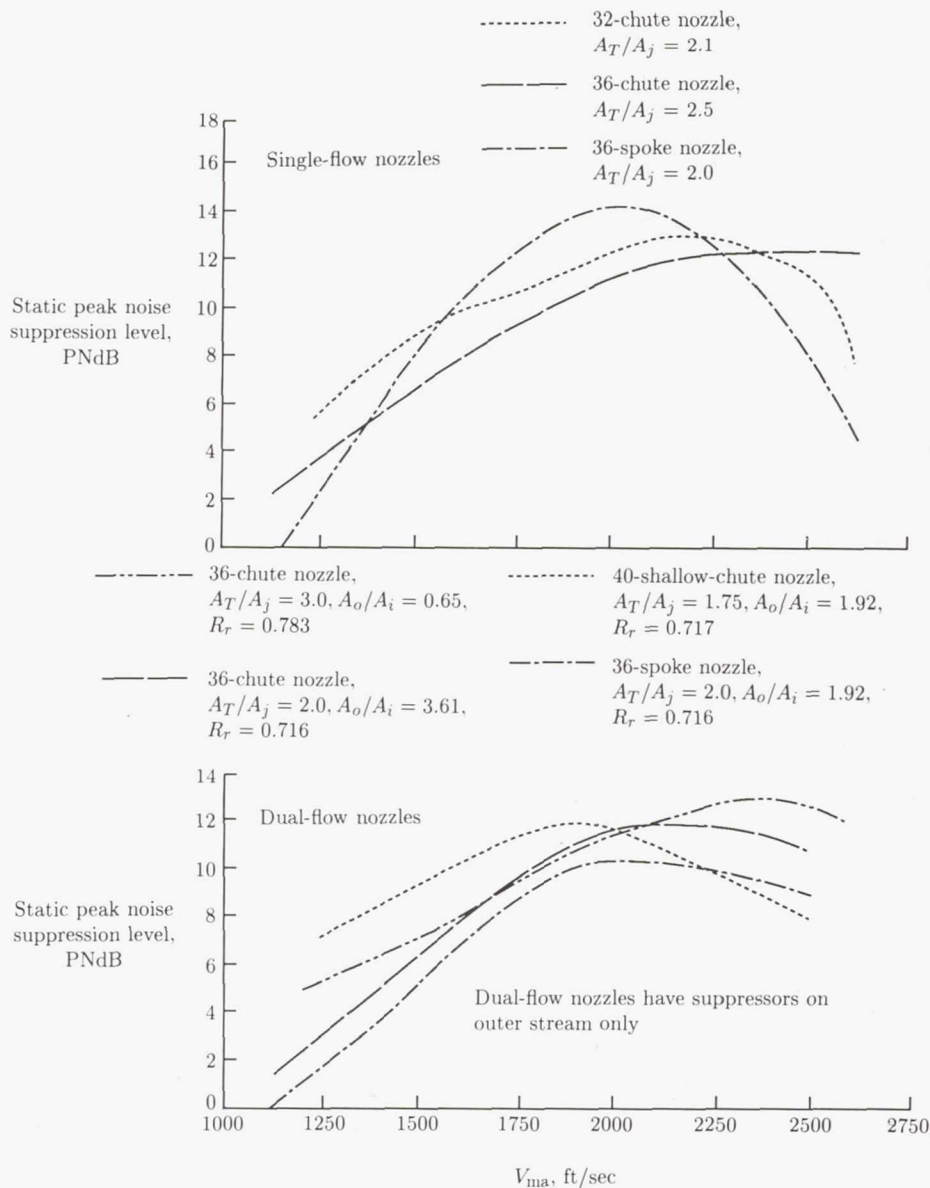
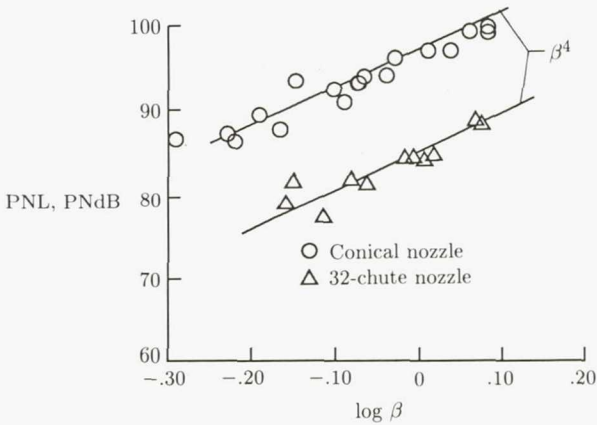


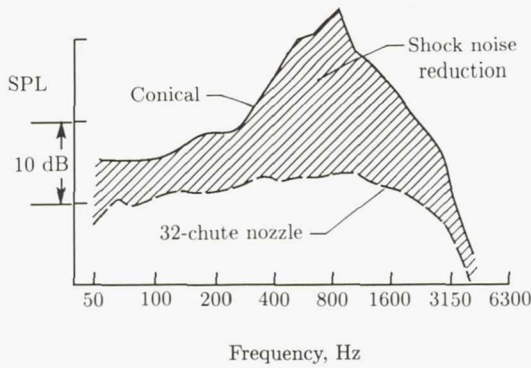
Figure 22. Typical static peak/PNL suppression characteristics of multi-element suppressors. 2400-ft sideline; standard day (59°, 70 percent relative humidity);  $A_T = 338 \text{ in}^2$ . (Based on ref. 20.)

Figure 21 shows the following two families of multi-element suppressors, for which a large body of data exists (ref. 20):

1. Single-flow applications for a turbojet or mixed turbofan and variable cycle engine (VCE)
2. Dual-flow applications with a suppressor in the high-velocity stream for a turbofan and VCE with inverted-velocity profile



(a) PNL at  $\theta_i = 50^\circ$ .



(b) SPL at  $\theta_i = 50^\circ$ ; 2400-ft sideline;  $V_j = 2300$  ft/sec;  $NPR = 3.2$ ; J-79 size.

Figure 23. Forward-quadrant shock noise reduction of 32-chute suppressor and conical nozzle. (From ref. 21.)

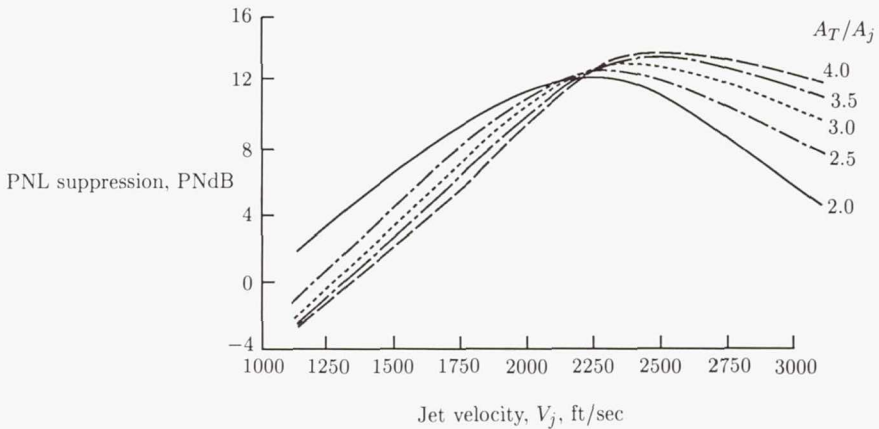
Figure 22 summarizes the suppression potential of various single- and dual-flow applications of multielement suppressor concepts in terms of static peak PNL suppression measured over the range of mass-averaged jet velocities  $V_{ma}$  covering typical takeoff, thrust cutback, and approach conditions. Single-flow applications generally exhibit slightly higher suppression than outer-stream suppressors on dual-flow systems, as the complete jet is segmented for single-flow applications. As an illustration of the potential of multielement suppressors for shock noise reduction, figure 23 (from ref. 21) shows the forward-quadrant noise reduction in terms of PNL at  $\theta_i = 50^\circ$  for a wide range of supersonic jet Mach numbers. Also shown are the spectral reductions for a 32-chute, single-stream suppressor compared with those for a conical nozzle.

Next, data trends obtained with geometric variations of multitube, multispoke, and multichute suppressors are presented. For multitube suppressors, the design variables having first order impact are

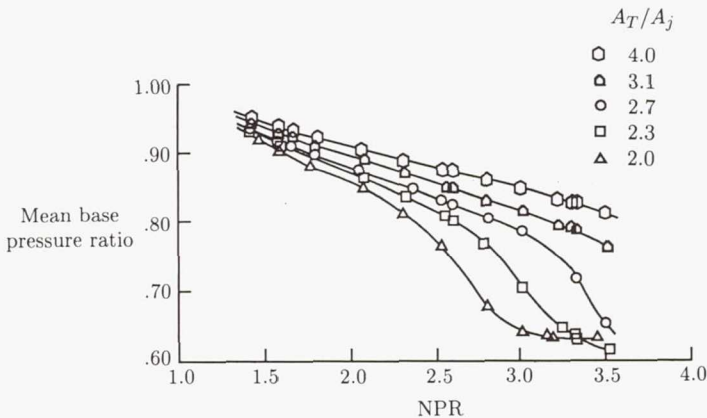
1. Suppressor area ratio (total area/flow area,  $A_T/A_j$ )
2. Number of tubes
3. Ratio of internal tube length to diameter,  $L_t/D_t$
4. Exit plane and base plane stagger

The influence of the above four design variables on both acoustic and aerodynamic performance (in terms of pressure levels in the base region) is shown in figures 24 to 27. The following trends are indicated.

At high jet velocities, higher area ratios yield higher levels of acoustic suppression than lower area ratios yield; at low jet velocities, the inverse is true. (See fig. 24.)



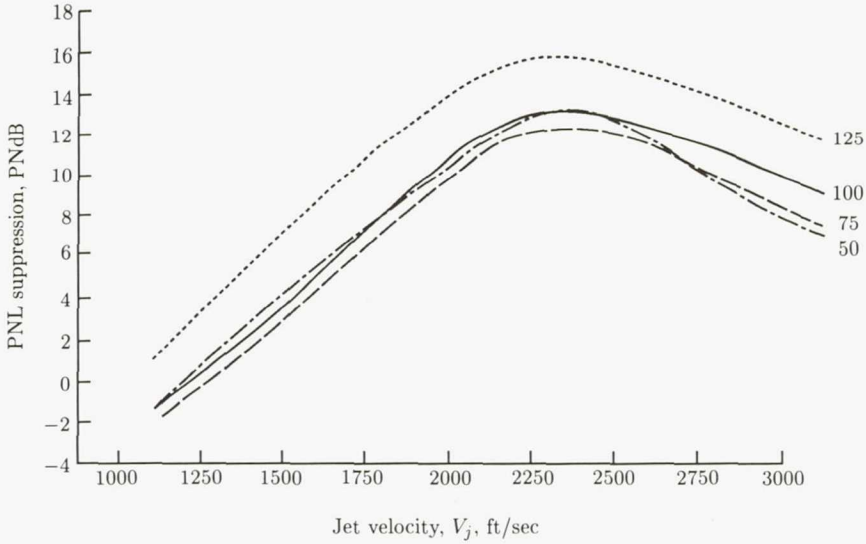
(a) PNL suppression; 1500-ft sideline; no shroud; based on data at  $A_T/A_j = 2.0, 2.3, 2.7, 3.1, \text{ and } 4.0$  (2.0 and 4.0 repeated).



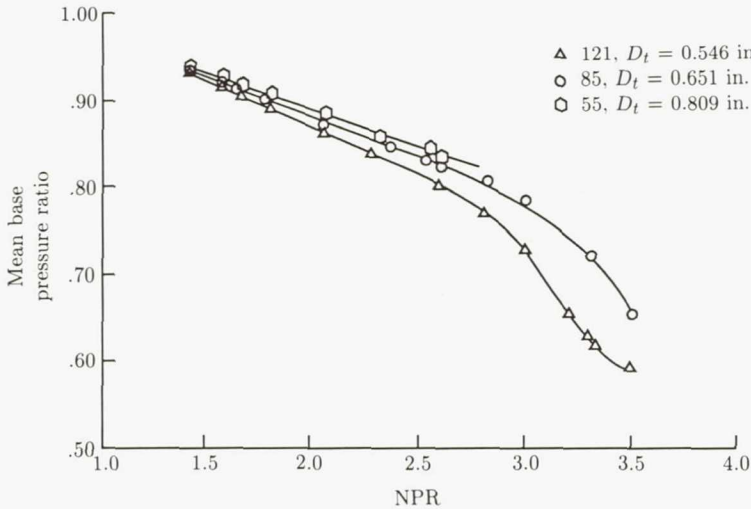
(b) Base pressure distribution; hot flow data.

Figure 24. Impact of multitube nozzle area ratio on acoustic and aerodynamic performance.  $L_t/D_t = 2.2$ . (From ref. 17.)

The designs with higher area ratios enhance ventilation of the base region to ambient air, the result being base pressures which approach the ambient pressure and thus base drag is reduced. However, increasing the area ratio requires a larger nozzle diameter and associated weight and drag penalties.



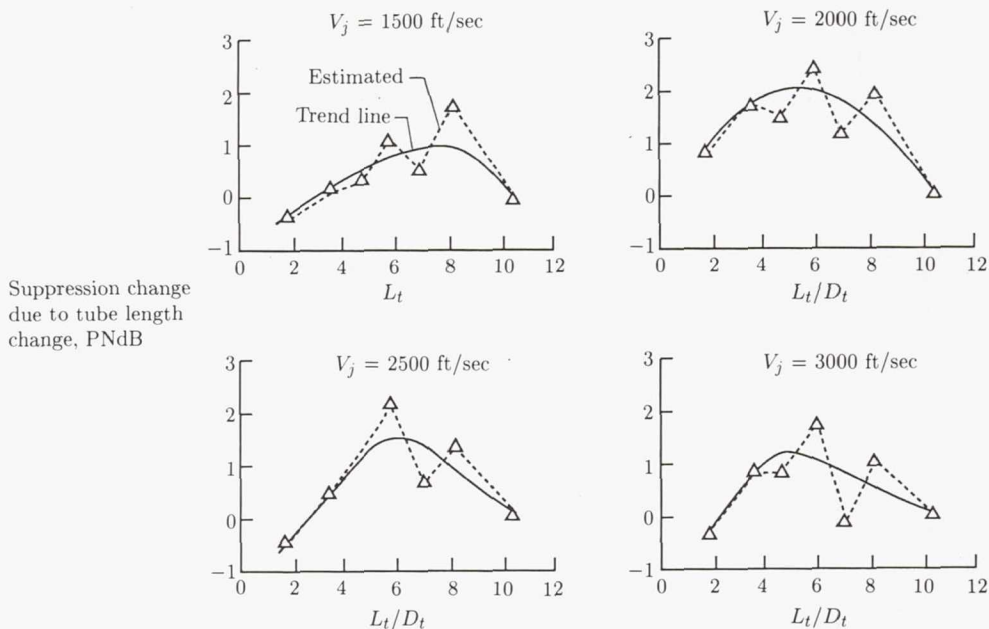
(a) Effect of number of holes; 1500-ft sideline; no shroud; based on data for 55, 85, and 121 holes (55 holes repeated).



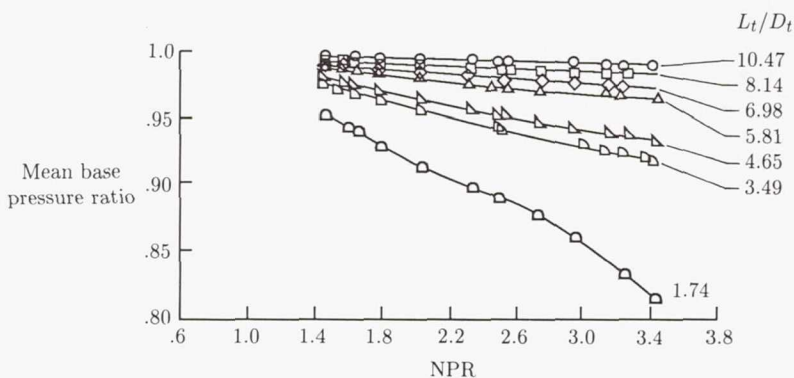
(b) Base pressure distribution; hot flow data.

Figure 25. Impact of multitube nozzle degree of segmentation on acoustic and aerodynamic performance.  $A_T/A_j = 2.7$ ;  $L_t/D_t = 2.2$ . (From ref. 17.)

For a given area ratio, increasing the number of tubes results in higher levels of noise suppression because of the shift of acoustic energy into higher frequencies. However, the increase yields lower base pressure for tubes in the interior because of poor ventilation and results in high base drag. (See fig. 25.)



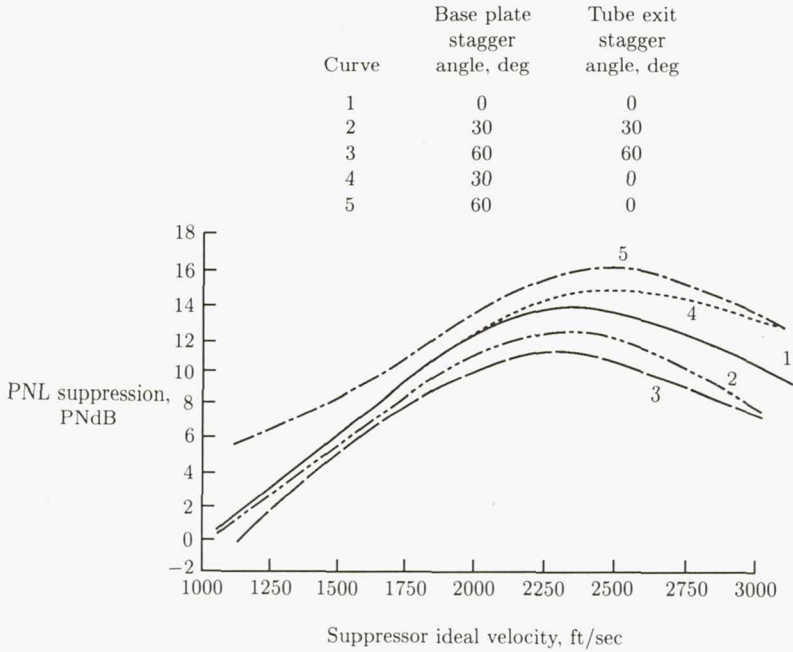
(a) Effect of tube internal length ratio on noise suppression; 300-ft sideline.



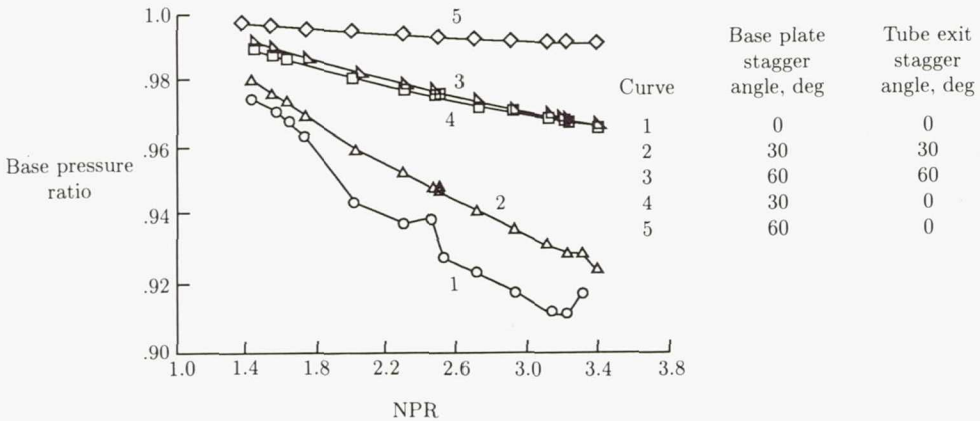
(b) Base pressure distribution.

Figure 26. Impact of multitube nozzle ratio of tube length to diameter on acoustic and aerodynamic performance.  $A_T/A_j = 3.19$ ; 85 tubes; no shroud. (From ref. 17.)

The data for the ratio of tube length to diameter indicate optimum PNL suppression as a function of jet velocity. (See fig. 26.) Long tubes enhance base ventilation by virtue of the distance available for entrainment of ambient air. However, weight and stowing for cruise determine the upper limit for this parameter.



(a) Acoustic performance; 1500-ft sideline;  $A_T/A_j = 2.27$ .



(b) Aerodynamic performance;  $A_T/A_j = 2.0$ .

Figure 27. Impact on multitube nozzle base and exit plane stagger on acoustic and aerodynamic performance. 72 plain tubes; no shroud. (From ref. 17.)

The data for exit plane and base plane stagger (fig. 27) indicate that jets with coplanar exits but large values of base plane stagger yield the largest levels of acoustic suppression and low values of base drag. Coplanar exits help establish a uniform coalescing of the individual jets to merge into a single jet. High values of base stagger result in adequate entrainment of ambient air for better mixing and diffusion of jets in the interior, the result being lower merged velocity and hence lower noise levels. Improved entrainment also results in lower base drag.

Chutes and spokes have similar geometric planforms, the only difference being that chutes have the capability of entraining the ambient air by means of the ventilation channel upstream of the nozzle exit plane and spokes do not. Hence, the multispoke suppressors yield lower aerodynamic performance than the multichute suppressors. Acoustic suppression potential of chutes and spokes is very similar. Figure 28 is a brief summary of the multichute and multispoke nozzle acoustic and aerodynamic performance trends with key geometric parameters, such as suppressor area ratio  $A_T/A_j$ , element number, and shape.

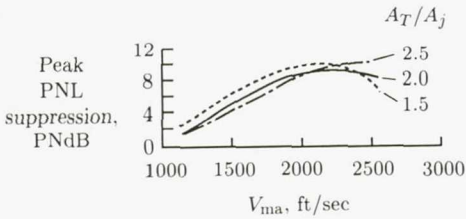
Chutes exhibit similar noise suppression trends with suppressor area ratio as the tubes, that is, higher area ratios yield more suppression at high jet velocities and the lower area ratios yield more suppression at lower jet velocities. (Compare figs. 28(a) and 24(a).) However, as the suppressor area ratio is increased, aerodynamic performance of chutes in terms of gross thrust coefficient<sup>1</sup>  $C_{f,g}$  deteriorates, a trend opposite to that of tubes. The principal reason for this deterioration is that as area ratio is increased for chutes, the base area is increasing for a given area available for entrainment of ambient air through the entrainment channels. (Compare figs. 28(b) and 24(b).) Acoustic suppression is a fairly weak function of number of chutes. (See fig. 28(c).) For a given suppressor area ratio and chute depth/width ratio  $D/W$ , the aerodynamic performance of the suppressor decreases with increases in chute number. The principal reason for this decrease is that as the chute number increases for a given suppressor area ratio, the chute widths decrease. Thus for a constant chute depth/width ratio, the chute depth decreases, the result being poorer ventilation of the chute in the interior and hence an increase in base drag. (See fig. 28(b).) Acoustic suppression levels obtained with chutes and with spokes are similar (fig. 28(d)), with a slightly higher level of suppression exhibited for chutes at high jet velocities.

Exit plane angle (canting) has a noticeable impact on both acoustic and aerodynamic performance. (See fig. 28(e).) A  $10^\circ$  cant helps the individual jets to retain their identity for a longer distance and thus helps improve shearing of the multiple jets by the ambient air to yield higher levels of acoustic suppression. However, a  $10^\circ$  cant tends to separate the flow from the plug surface, the result being poor aerodynamic performance.

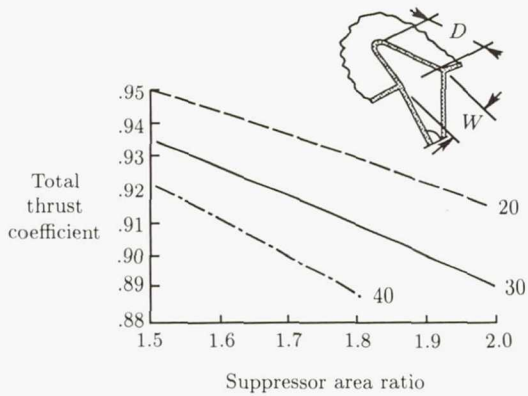
Planform shape of the spokes (i.e., tapered or parallel-sided) affects both acoustic and aerodynamic performance. (See fig. 28(f).) Parallel-sided spokes yield a larger flow perimeter for shearing by ambient air and thereby yield higher levels of acoustic suppression than the tapered spokes. Aerodynamic performance of parallel-sided spokes is lower than that of tapered spokes since parallel-sided spokes have larger base areas in the interior, where ambient air cannot conceivably penetrate.

---

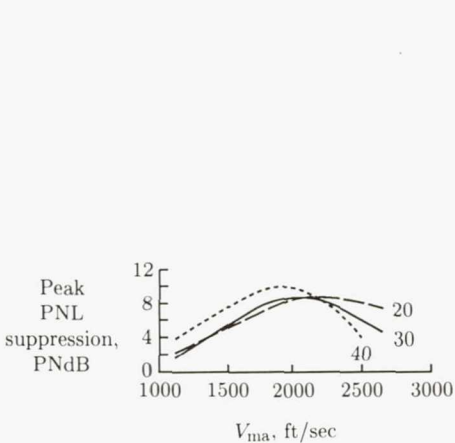
<sup>1</sup> Gross thrust coefficient  $C_{f,g}$  is defined as the ratio of actual gross thrust to ideal thrust based on isentropic expansion to ambient pressure.



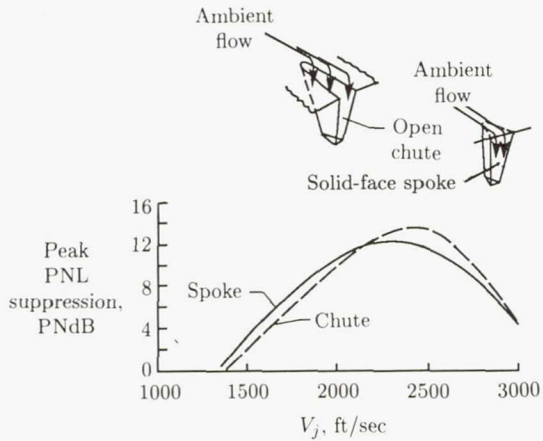
(a) Influence of 36-chute suppressor area ratio on peak PNL suppression; 2400-ft sideline; dual flow; scaled to  $A_T = 338 \text{ in}^2$ .



(b) Variation of total thrust coefficient with suppressor element number and area ratio; single-flow plug nozzle;  $D/W = 1.0$ ;  $M = 0.36$ ;  $15^\circ$  plug angle.



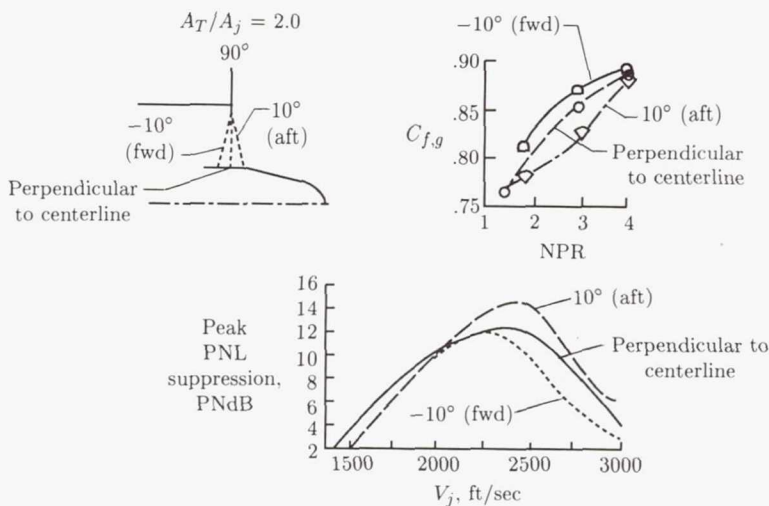
(c) Peak PNL suppression as function of suppressor element number; static;  $A_T/A_j = 1.75$ ;  $R_r = 0.717$ ; scaled to  $A_T = 338 \text{ in}^2$ .



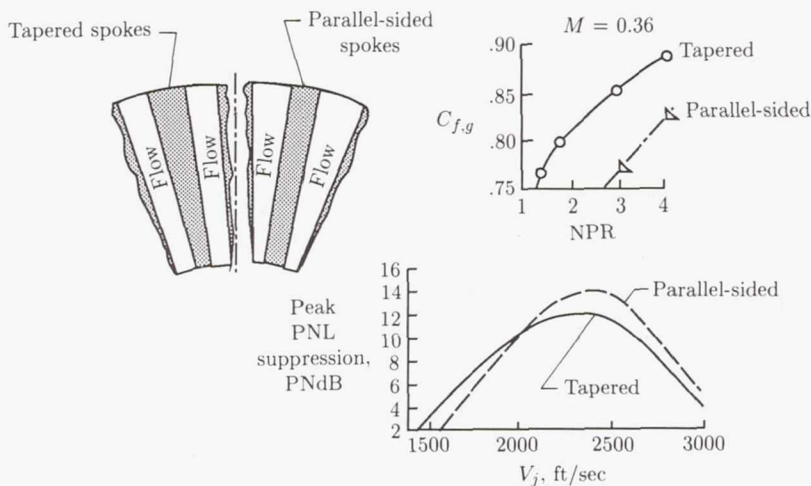
(d) Acoustic suppression of chute and spoke suppressors; 1500-ft sideline; 32 elements;  $A_T/A_j = 2.0$ ;  $R_r = 0.498$ .

Figure 28. Multichute and multispoke suppressor nozzle acoustic and aerodynamic performance trends. (From ref. 20.)

Figure 29 summarizes the acoustic suppression versus thrust degradation for various tube, spoke, chute, plug, coannular, and ejector nozzles. Cruise performance



(e) Influence of element cant angle on acoustic and aerodynamic performance.



(f) Influence of element planform shape on acoustic and aerodynamic performance.

Figure 28. Concluded.

considerations certainly will require that the suppressors be stowed to minimize mission impact. Typical schemes for stowage and deployment of chutes and tubes are conceptually illustrated in figure 30.

The above discussion indicates that multielement suppressor design involves a complex interaction of acoustic suppression potential, aerodynamic performance,

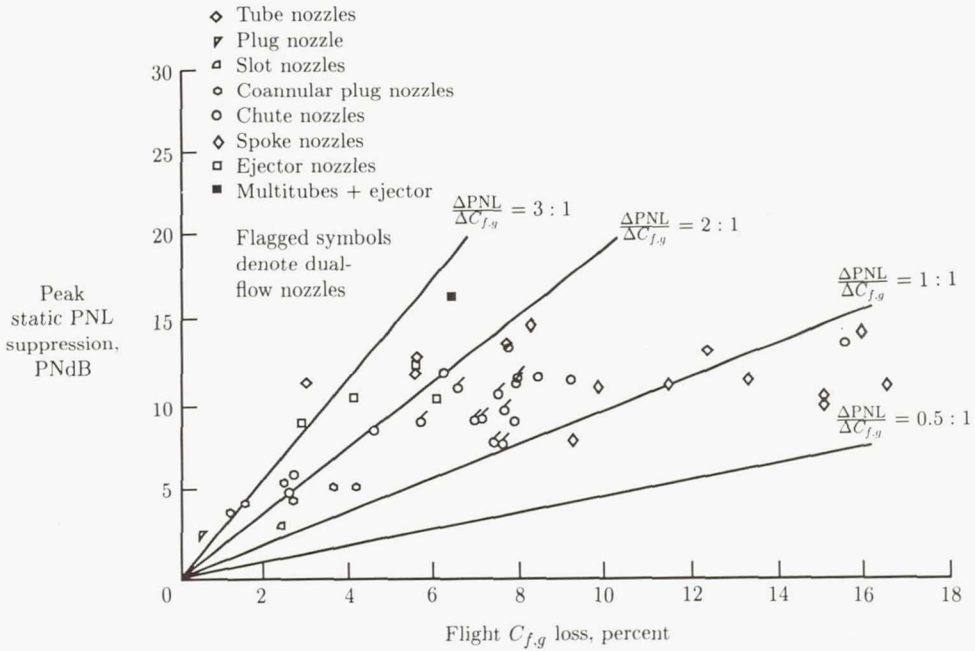


Figure 29. Generalized flight performance and static suppression levels relative to conical nozzle. Based on measured aerodynamic performance and acoustic data. Nominal conditions: single flow— $V_{ma} \approx 2400$  ft/sec and  $NPR \approx 3.0$ ; dual flow— $V_{ma} \approx 2200$  ft/sec,  $NPR_o \approx 3.0$ , and  $NPR_i \approx 2.5 \rightarrow 3.5$ . (From ref. 20.)

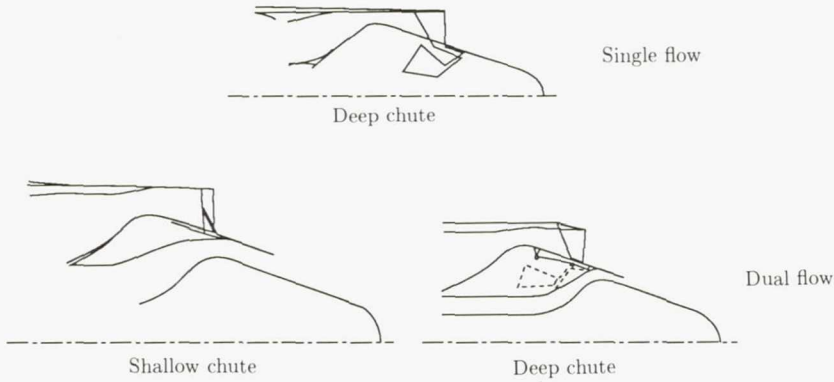


Figure 30. Installation schemes for stowed and deployed multielement suppressors. (From ref. 20.)

and mechanical feasibility (i.e., implementation, stowability, and reliability). The ultimate impact of these considerations on the mission is equally important.

### *Ejectors*

An ejector, when designed as an integral part of the propulsive nozzle system, can yield optimum aerodynamic performance for the entire mission by providing an optimum flow expansion surface. It can also provide additional noise suppression than a nozzle system without an ejector by virtue of its capability for induction of ambient air to enhance mixing and shielding or suppression of noise sources within the ejector length. For an extensive discussion of the principles of noise reduction by mixing nozzles and ejector nozzles, see reference 22. Ejectors used in conjunction with conical nozzles or basic coannular plug nozzles have been ineffective since the dominant acoustic sources are located outside the ejector. However, for suppressor nozzles, the dominant acoustic sources are located close to the jet exit plane; hence, ejectors with acoustic treatment on the internal flow surface effectively improve the basic suppressor acoustic performance. Air induction by ejectors is also more effective, as induced air can impact mixing in the region of dominant acoustic sources.

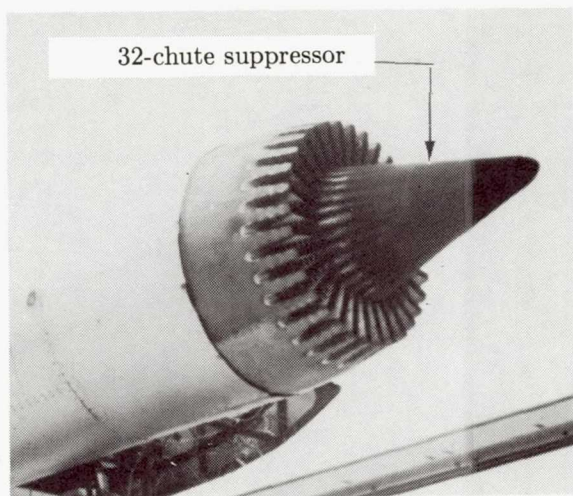
Flight tests on a Viper turbojet engine fitted with various exhaust suppressors with and without treated ejectors are reported in reference 23. A maximum attenuation of 14 EPNdB was measured at an ideal jet exhaust velocity of 732 m/sec (2400 ft/sec) at an adjusted altitude of 152 m (500 ft).

In reference 24, researchers used a short ejector lined with bulk absorber on a 32-deep-chute primary nozzle system installed on a J-79 dry turbojet engine (nonaugmented; see fig. 31(a)). The short ejector attained a nearly uniform 2 dB more peak PNL suppression than the suppressor alone. (See fig. 31(b).) In a more extensive scale-model program sponsored by NASA Lewis Research Center (ref. 25), researchers investigated the influence of ejector geometry and acoustic treatment on acoustic and aerodynamic performance. The scale-model system employed a 20-chute outer annular suppressor with inverted-velocity profile and an ejector with or without acoustic treatment. The plug surface was both hard walled and acoustically treated.

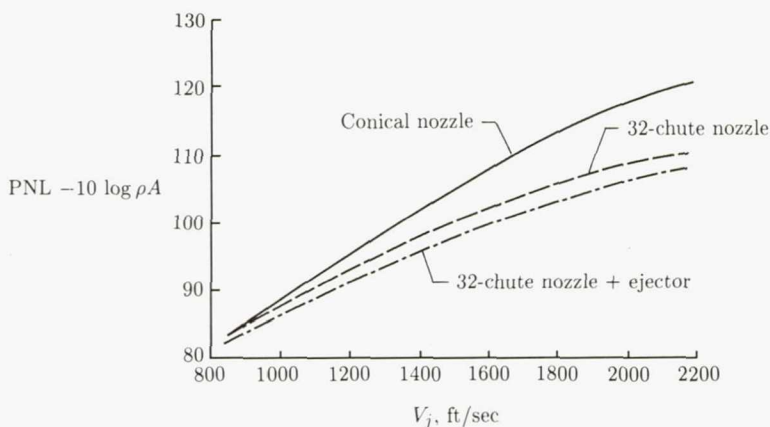
Influence on ejector spacing  $S$  from the suppressor exit plane (normalized by the equivalent diameter based on flow area  $D_{eq}$ ) on peak PNL as a function of mass-averaged jet velocity is shown in figure 32. The influence of ejector spacing on aerodynamic performance in terms of thrust loss due to chute base drag as a function of outer stream pressure ratio is shown in figure 33. Increasing the ejector spacing results in a marked improvement in the aerodynamic performance because an increased induction of ambient air into the chutes is possible with more spacing. This increased entrainment of ambient air results in improved mixing within the ejector system, and this mixing results in a lower merged velocity and hence lower noise levels.

Figures 34 and 35 show the influence of ejector length  $L$  on peak PNL and on thrust loss due to base drag. Increased ejector length yields slightly higher noise suppression at all jet velocities because of the containment of sources over a larger distance. The longer ejector shows improved aerodynamic performance as well.

Influence of acoustic treatment attached to the ejector internal surface and/or plug on acoustic characteristics is shown in figure 36. Successive treatment of the ejector and plug surfaces improves acoustic suppression. The hard-wall ejector provides the suppression by pure physical shielding and ambient air induction. Successive improvements because of the treatment are not very sensitive to treatment impedance.



(a) Suppressor installed on J-79 engine.



(b) Peak PNL's. 2128-ft sideline; full scale; scale factor, 2:1.

Figure 31. General Electric 32-chute annular nozzle on J-79 testbed with and without treated ejector. (From ref. 17.)

Based on these studies, the following design guidelines have evolved:

1. An increase in the axial stagger between the suppressor exit plane and the ejector improves acoustic and aerodynamic performance; however, weight and mechanical complexity increase.
2. An increase in ejector length improves noise suppression slightly.
3. Treatment of the ejector and the plug surface improves noise reduction potential, and the improvement is not sensitive to treatment impedance.

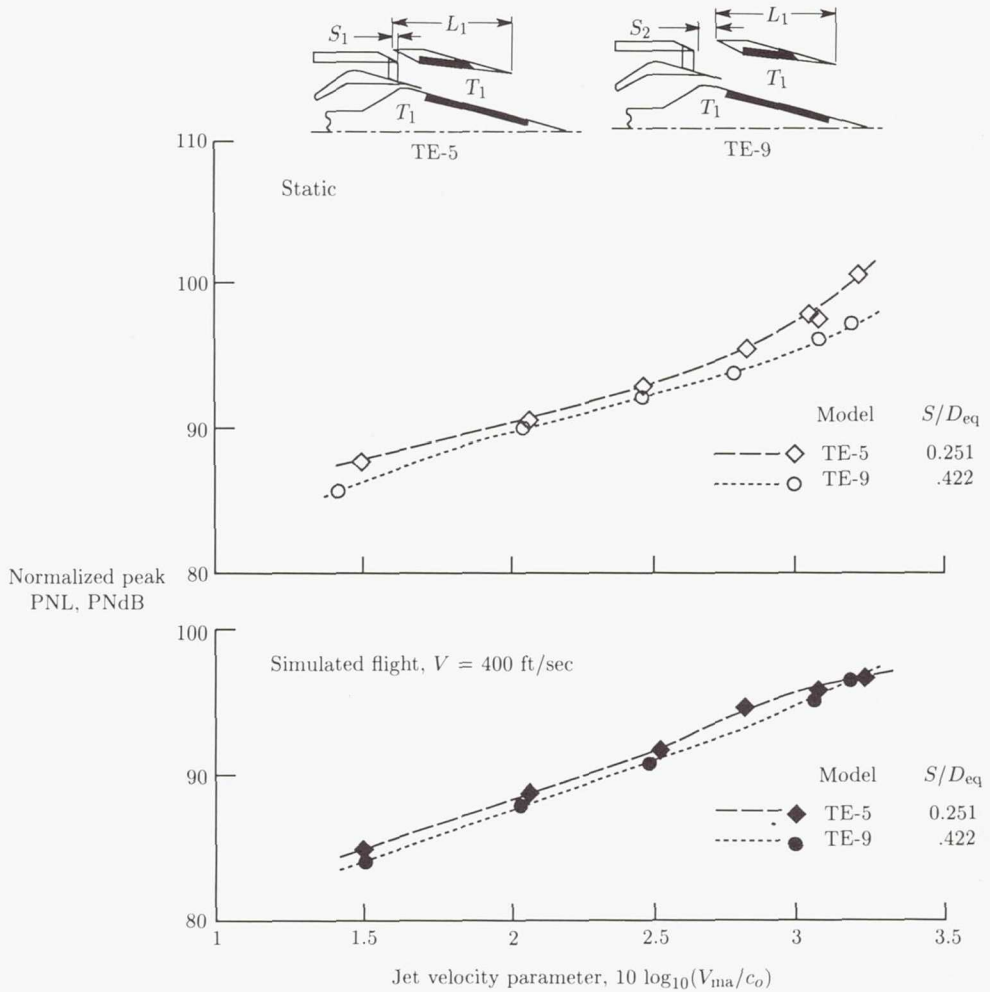


Figure 32. Influence of ejector spacing on normalized peak PNL of 20-shallow-chute suppressor nozzle (dual flow). 2400-ft sideline;  $A_T = 1400$  in<sup>2</sup>; standard day (59° F, 70 percent relative humidity). (Based on ref. 25.)

#### Annular Plug and 2-D Nozzles

Two-dimensional nozzles and plug nozzles with a high radius ratio  $R_r$  (i.e., ratio of inner radius to outer radius  $R_r$ ) exhibit similar flow characteristics near the jet exit plane, since a 2-D nozzle of height  $h$  and width  $b$  can be viewed as an "unwrapped" annular nozzle of annulus height  $h$  and of circumference  $b$ . However, the flow characteristics downstream and acoustic characteristics of these two types of nozzles are quite dissimilar. They are grouped herein under one section since they both serve as the first step in departure from the simple conical nozzles to achieve jet noise suppression.

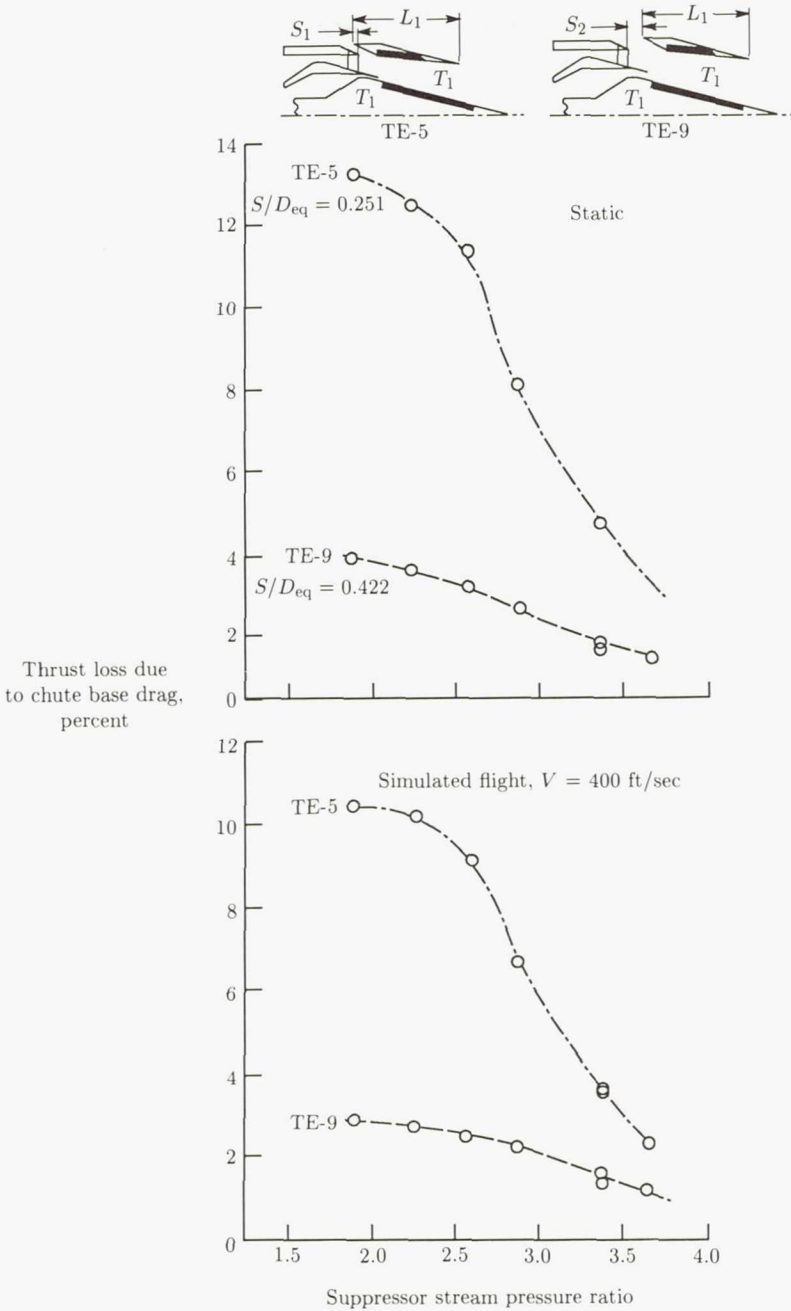


Figure 33. Influence of ejector spacing on base drag of 20-shallow-chute suppressor nozzle (dual flow). (Based on ref. 25.)

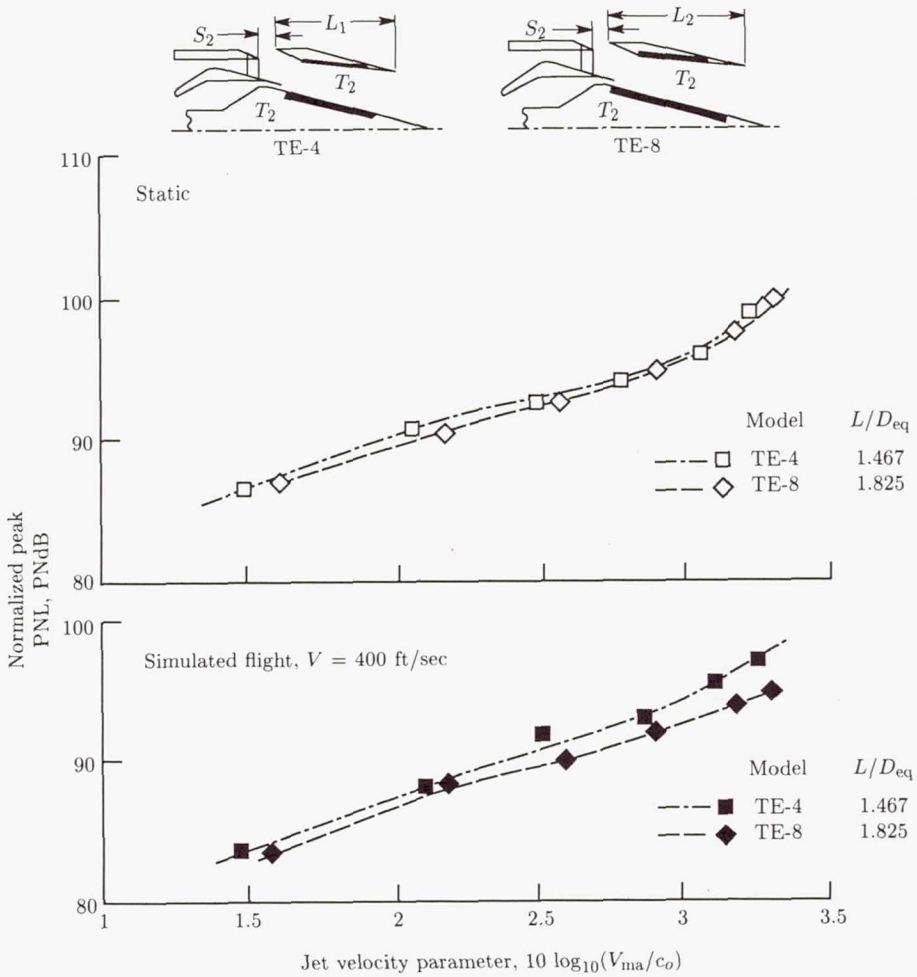
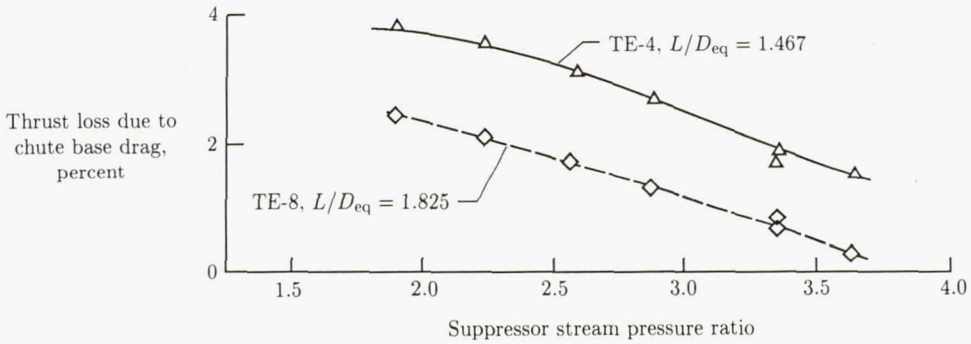


Figure 34. Influence of ejector length on normalized peak PNL of 20-shallow-chute suppressor nozzle (dual flow). 2400-ft sideline;  $A_T = 1400 \text{ in}^2$ ; standard day (59° F, 70 percent relative humidity). (Based on ref. 25.)

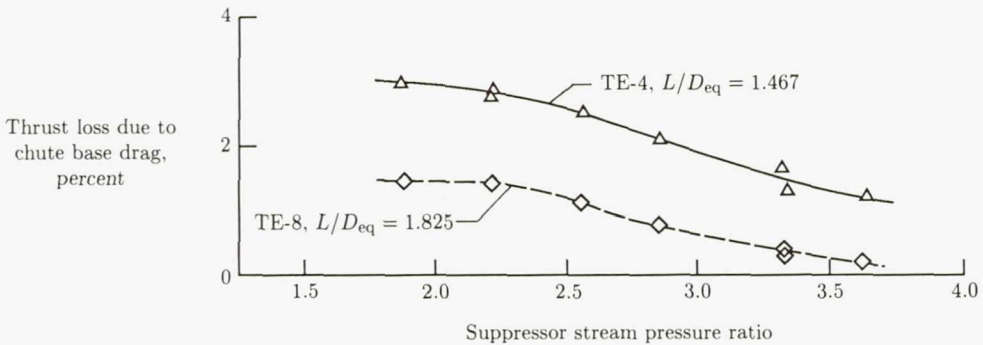
For a given flow area, as the plug nozzle radius ratio increases, annular height decreases and outer radius of nozzle increases. The noise reduction capability of plug nozzles is ascribable to the following:

1. Larger surface area is available for shear with ambient air than in the conical nozzle.
2. Additional surface (i.e., plug) is available for shearing the jet.
3. Smaller characteristic dimension (i.e., annulus height) is present in the high-jet-velocity region, and this smaller dimension implies the jet decay and shock structures are governed by annulus height rather than by the equivalent-flow-area circular nozzle diameters close to the exit plane. The annulus height being the characteristic dimension in the high-velocity region results in an acoustic power level spectrum with more high-frequency content than for

a circular nozzle. As in the case with multielement suppressors, the high-frequency acoustic content suffers larger atmospheric attenuation with plug nozzles than with circular nozzles to yield the observed noise reductions.



(a) Static.



(b) Simulated flight,  $V = 400$  ft/sec.

Figure 35. Influence of ejector length on base drag of 20-shallow-chute suppressor nozzle (dual flow). (From ref. 25.)

Figure 37 (from ref. 26) shows the noise reduction characteristics of annular plug nozzles compared with those of the conical nozzle over a range of jet velocities in the aft quadrant (shown as normalized peak OASPL), which is dominated by jet noise, and in the forward quadrant (shown as normalized  $50^\circ$  OASPL), which is dominated by broadband shock-cell noise. As radius ratio  $R_r$  increases, the normalized peak OASPL decreases. The trend of shock-cell noise (normalized  $50^\circ$  OASPL) with radius ratio is not very clear. High-radius-ratio plug nozzles which have a blunt tip tend to have two shock structures at high pressure ratios, one on

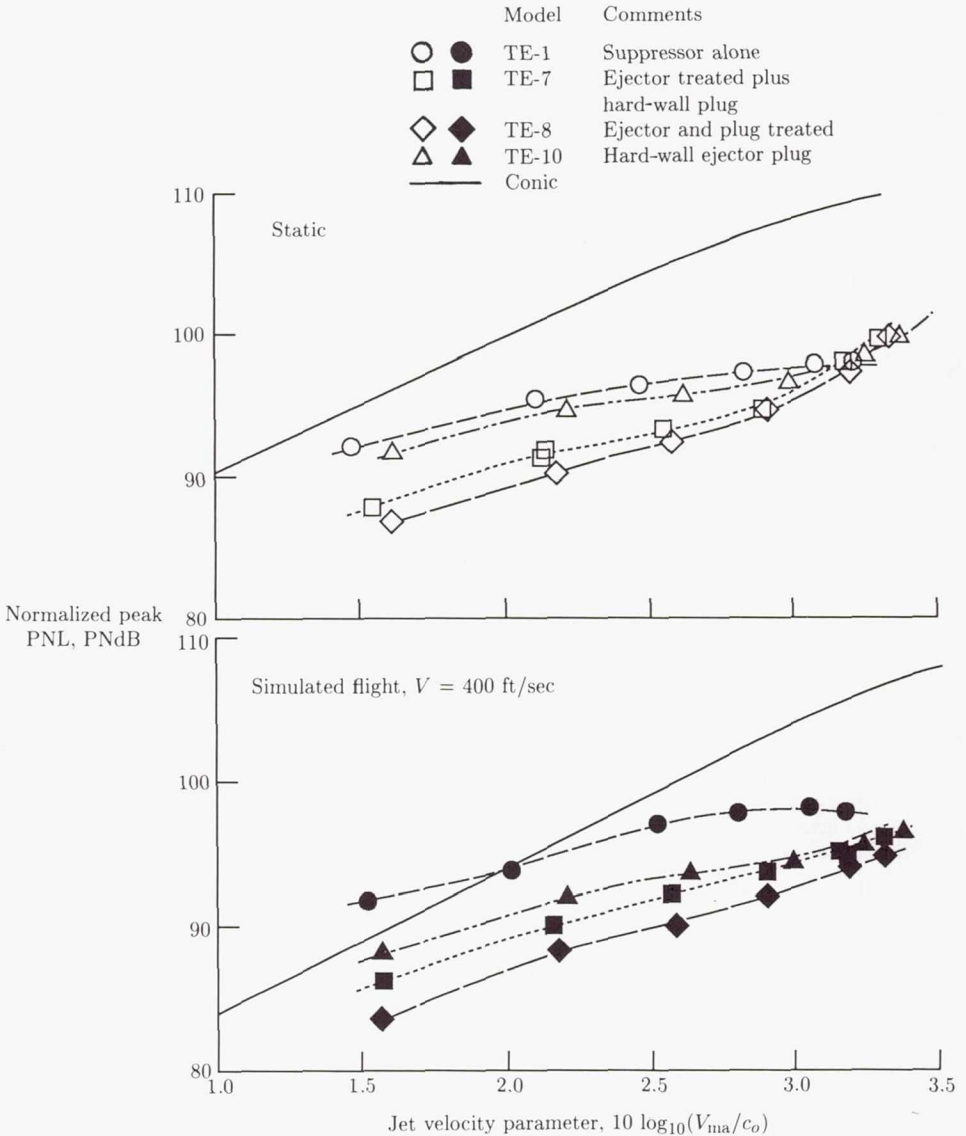
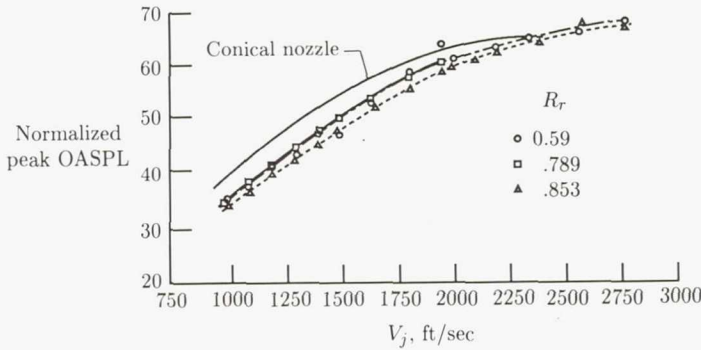


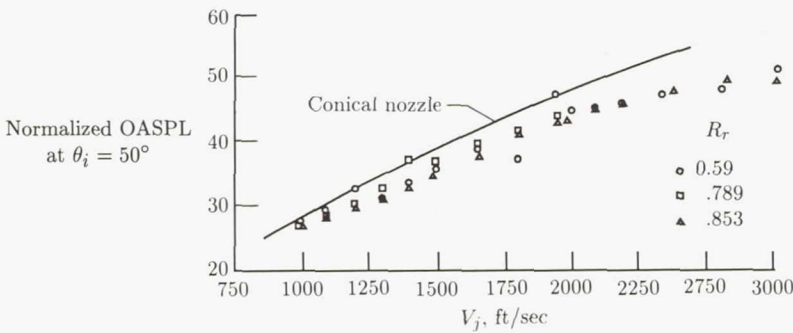
Figure 36. Influence of acoustic treatment attached to ejector and/or plug surface on peak PNL of 20-shallow-chute suppressor nozzle (dual flow). 2400-ft sideline;  $A_T = 1400 \text{ in}^2$ ; standard day (59° F, 70 percent relative humidity). (From ref. 25.)

the plug surface (characterized by annulus height) and another downstream of the plug surface due to a supersonic flow expansion fan around the blunt tip. When the downstream shock gets reflected from the jet shear layer it induces a train of shock-cell structures downstream of the plug. The downstream shock structure is typically characterized by the equivalent circular nozzle diameter. Thus, the shock

noise contribution observed at  $\theta_i = 50^\circ$  consists of contributions from both these two shock structures and a clear trend with radius ratio is absent.



(a) Peak OASPL.



(b) OASPL at  $\theta_i = 50^\circ$ .

Figure 37. Annular plug nozzle acoustic characteristics as function of radius ratio. 2400-ft sideline;  $A_T = 338 \text{ in}^2$ . (From ref. 26.)

High-radius-ratio plug nozzles have preferred noise characteristics. However, a higher radius ratio for a given flow area dictates a larger nacelle diameter with the accompanying weight and nozzle afterbody drag penalties. A value of 0.853 is considered to be the practical limit for the radius ratio. Elimination of shock structures on the plug surface and downstream of the plug is discussed in the section entitled *Shock Noise Control*.

Two-dimensional nozzles (also called rectangular nozzles) are gaining applications in military aircraft because of their thrust-vectoring capability. Two-dimensional nozzles are characterized by their aspect ratios (defined as width/height). At sufficiently high aspect ratios (typically larger than 6), the flow near the exit plane of the jet exhibits a 2-D character. Two-dimensional nozzles tend to be generally quieter

than equivalent circular conical nozzles, essentially because of the increased surface area available for shear with the ambient air compared with that of an equivalent circular conical nozzle. Two-dimensional nozzles exhibit azimuthal variation and the plane containing the minor axis is louder than the plane containing the major axis, particularly in the high-frequency region. The 2-D jet flow loses its 2-D nature at downstream locations because of jet diffusion, and at distances sufficiently downstream the flow becomes a circular jet. Since low-frequency noise of jets is associated with large, turbulent eddies and large, turbulent eddies of 2-D nozzles are at regions where the jet is circular, low-frequency noise of 2-D jets typically does not show any azimuthal variation.

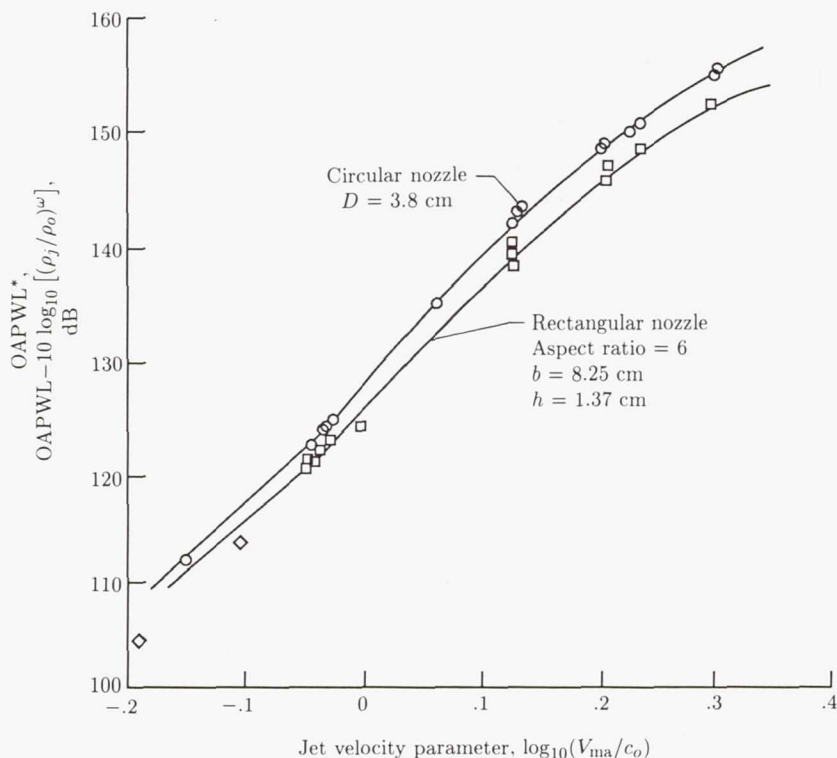


Figure 38. Overall power levels (OAPWL) of circular and rectangular nozzles. (From ref. 9.)

Scale-model tests were performed on rectangular jets (ref. 9), and some of the results are presented in figures 38 and 39 to justify the statement made above. Increasing the aspect ratio of a 2-D nozzle for a constant flow area results in the jet flow retaining its planar nature for larger distances. Also, increasing the aspect ratio for a given flow area reduces the jet height and thus results in a larger velocity gradient in the vertical direction. This larger velocity gradient in turn yields a faster decay of the jet, although the strength of the high-frequency sources (close to the jet exit plane) increases. Reduction in height also results in smaller shock cells, the structure of which extends to a smaller physical length. The smaller shock cells result in lower shock noise levels. Thus, increasing the aspect ratio of a 2-D

nozzle is beneficial acoustically. Mechanical considerations involving airframe-engine integration might limit the aspect ratio.

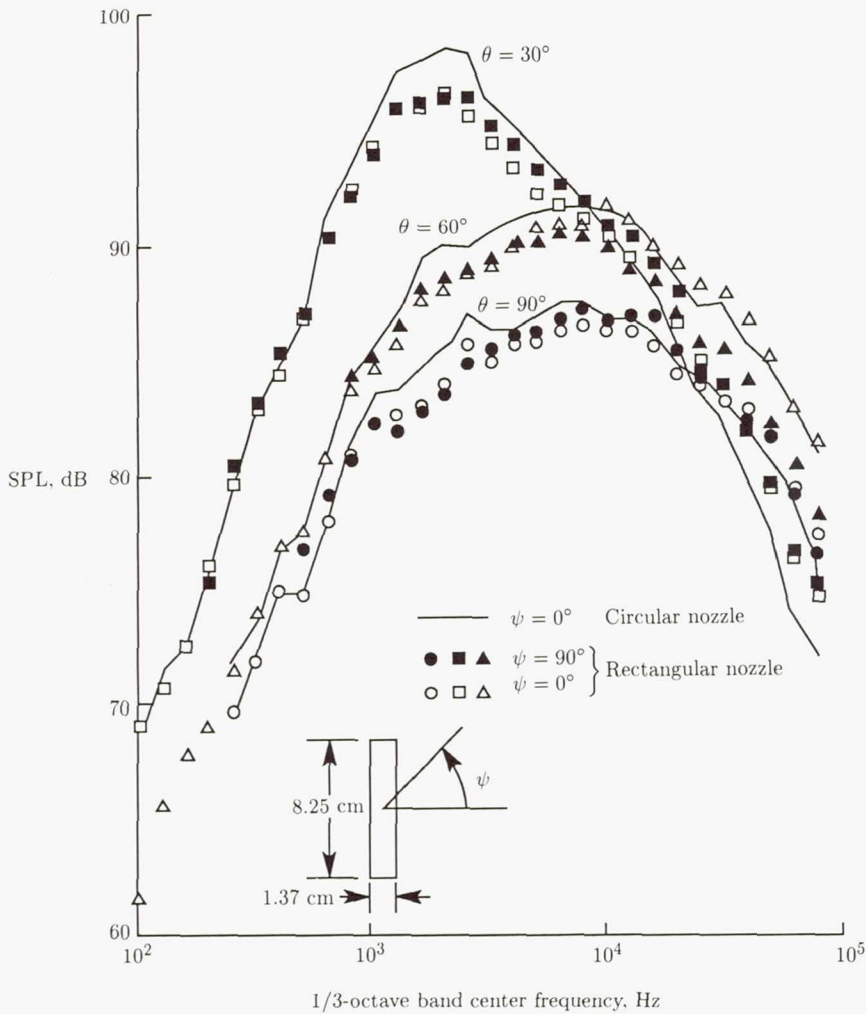


Figure 39. Spectral characteristics of circular and rectangular nozzles.  $V_j = 966$  ft/sec;  $T_o = 528^\circ R$ . (From ref. 9.)

### Aerothermodynamics Concepts

#### Inverted Flow

The inverted-flow concept employs a nozzle system wherein the cooler, lower velocity jet is surrounded by the hotter, higher velocity jet. This arrangement is the inverse of a conventional turbofan nozzle system. By surrounding the hotter, higher velocity jet on one side by the cooler, lower velocity jet and on the other side

by the ambient airstream, one is generating a mean velocity gradient (and hence shearing stress) on both sides of the principal noise-generating jet which results in a faster decay of the jet plume. However, as noted with multielement suppressors or plug nozzles, higher shear stress in the vicinity of the jet exhaust plane results in higher acoustic source strength close to the jet exhaust plane (high-frequency content), and by virtue of atmospheric absorption this results in lower perceived noise levels in the far field. A faster decaying jet has a lower contribution to the low-frequency portion of the spectrum. The application of a high-radius-ratio plug nozzle in conjunction with an inverted-velocity profile accentuates the shifting of acoustic energy into higher frequencies.

Figure 40 presents data from reference 27. Figure 40(a) shows a design concept for obtaining an inverted-flow-velocity profile in conjunction with a high-radius-ratio plug nozzle. Figures 40(b) and 40(c) show acoustic data in the aft and forward quadrants in terms of PNL for various combinations of plug radius ratio and inner/outer area ratios  $A_i/A_o$  over a range of mass-averaged jet velocities ( $V_{ma} = \frac{w_o v_o + w_i v_i}{w_o + w_i}$ ) and also over a range of "averaged" shock strength parameters  $\beta$ . This parameter is defined as  $\sqrt{M^2 - 1}$ , and  $M$  is based on mass-averaged flow conditions. Substantial reductions in jet as well as shock-cell broadband noise are shown for the coannular nozzle for a wide range of plug radius ratios and area ratios.

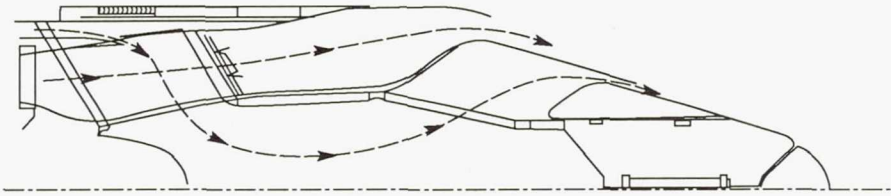
Figures 40(d) and 40(e) show the noise reduction potential of a representative coannular nozzle ( $A_i/A_o = 0.2$  and an outer stream radius of 0.853) in terms of PNL directivity and of spectral characteristics at three observer angles. Acoustic suppression in the aft quadrant and at  $90^\circ$  is attributable to the jet source modification by the inverted flow, whereas suppression in the forward quadrant is attributable to the modified shock structure (i.e., one set of shock cells on the plug and another set of shock cells downstream of the plug).

The inherent acoustic suppression associated with the inverted-flow concept has been demonstrated in a design wherein a duct burner in the fan stream accelerates the fan stream to a velocity higher than that of the core stream. (See ref. 28.)

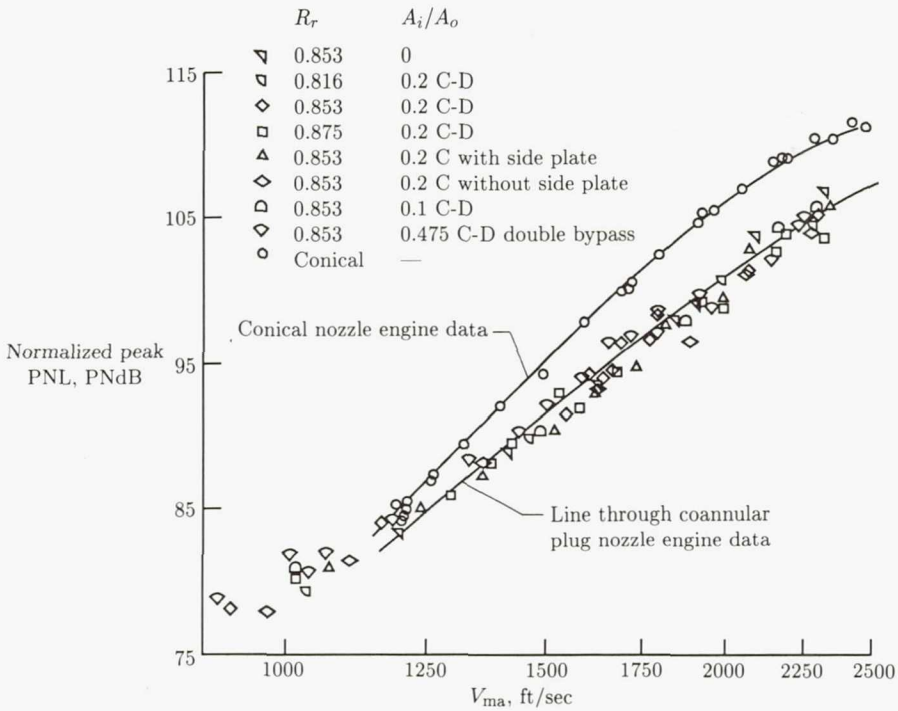
### *Thermal Acoustic Shield*

A high-temperature, low-velocity gas stream (termed a thermal acoustic shield, TAS) surrounding the principal jet yields jet noise reduction because of the acoustic wave refraction and reflection that occurs due to the impedance change at the interface between the principal jet and the TAS. Figure 41 (from ref. 29) schematically illustrates the concept of TAS wherein the high-frequency noise that is generated near the jet exit plane is either refracted away from the observer or undergoes multiple reflections within the TAS, and a weakened acoustic signal reaches the observer. Certain combinations of the velocity and speed of sound in the principal jet and the TAS yield a total internal reflection of the sound from the observer. The condition for total internal reflection is given by Snell's law as applied to the moving media.

The noise reduction potential of the TAS decreases for sources which are located far downstream from the jet exit plane since the TAS mixes with the principal jet and thereby is not able to maintain a sufficient level of discontinuity in the acoustic impedance. In other words, the TAS is not effective in reducing low-frequency noise.



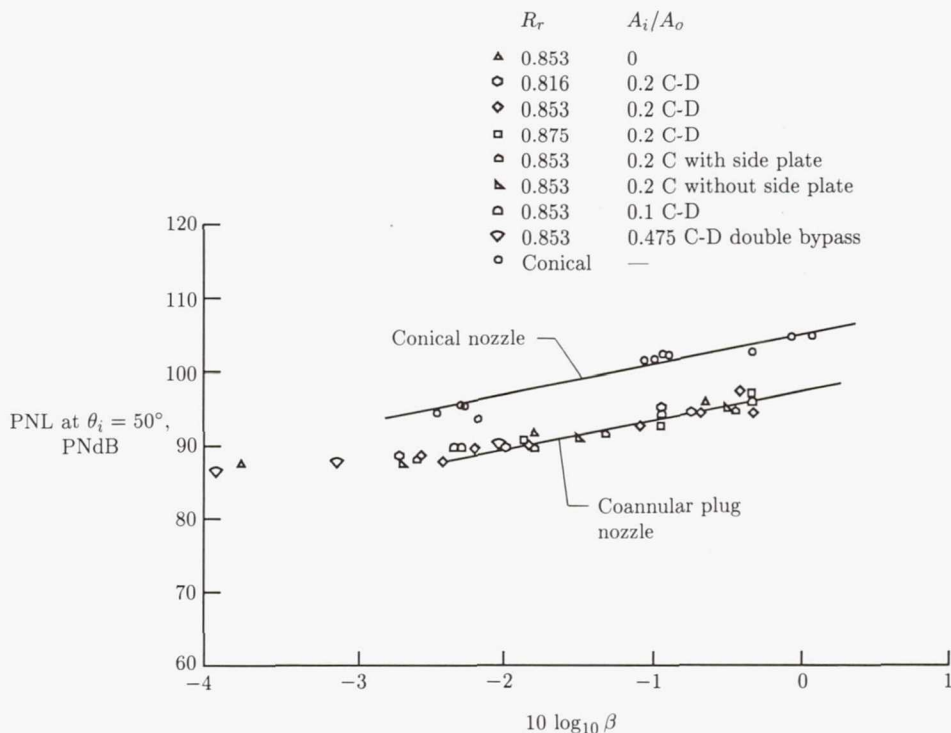
(a) Schematic.



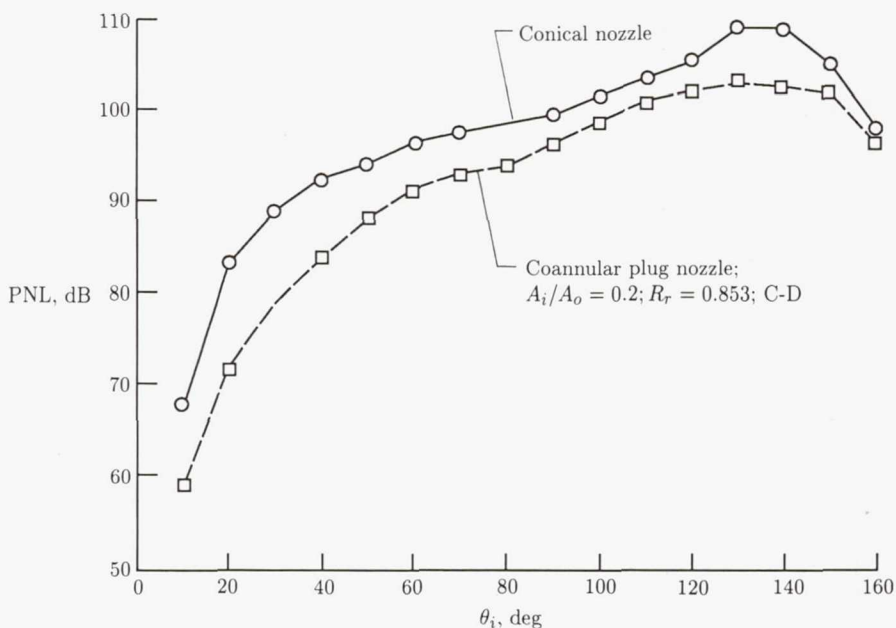
(b) Peak PNL for various radius ratios and area ratios.

Figure 40. Schematic and acoustic characteristics of coannular nozzles with inverted-velocity profile. 2400-ft sideline;  $A_T = 1400 \text{ in}^2$ . (From ref. 27.)

Thus, the TAS concept is more effective when used in conjunction with multielement suppression concepts which have a dominant high-frequency content.

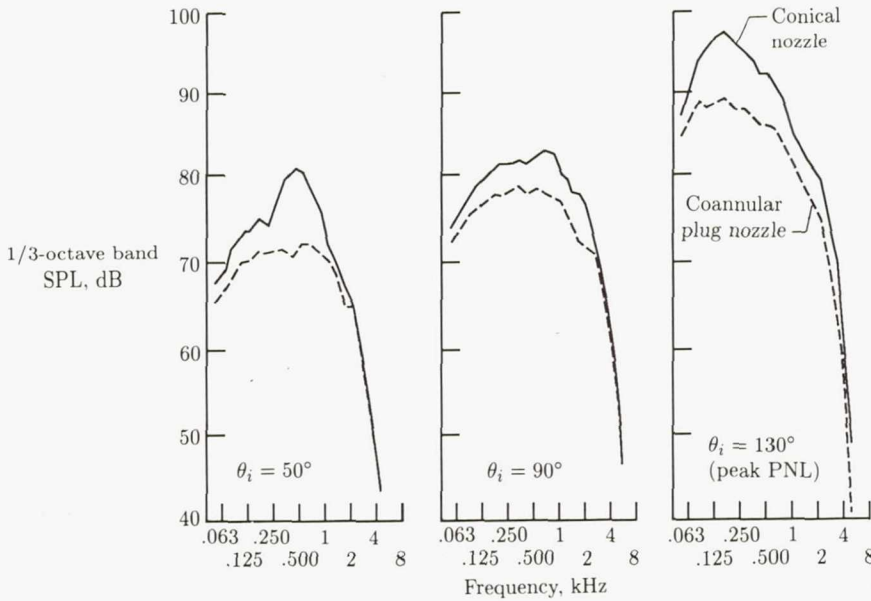


(c) PNL at  $\theta_i = 50^\circ$  for various radius ratios and area ratios.



(d) PNL directivity characteristics.

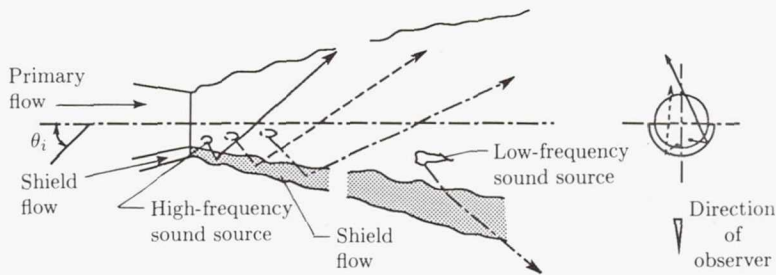
Figure 40. Continued.



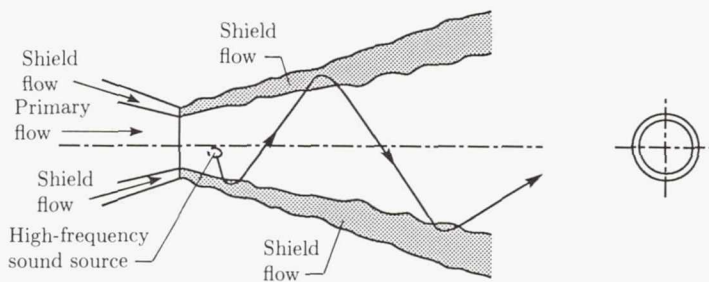
(e) Spectral characteristics.

Figure 40. Concluded.

Early experimental investigations of the TAS concept for unsuppressed nozzles (refs. 30 to 32) have shown impressive reductions in noise levels. Further detailed studies (refs. 29 and 33) involved TAS applications to single- and dual-flow nozzles with and without multichute suppression devices. Results from application of a  $180^\circ$  shield on an annular plug nozzle with a radius ratio of 0.85 and to a 32-chute annular plug suppressor with a suppressor radius ratio of 0.62 are shown in figure 42. The data show spectral suppression obtained by the TAS for typical advanced supersonic transport (AST) approach, cutback, and takeoff cycle conditions. Very significant suppression of high-frequency noise in the aft quadrant is shown with the  $180^\circ$  shield applied to both systems. The sharp increase in suppression in the aft quadrant ( $\theta_i \geq 120^\circ$ ) is due to a total internal reflection of the sound waves of the primary jet by the shield. Noise suppression occurs in the forward quadrant and at  $\theta_i = 90^\circ$  because velocity and temperature gradients of the core jet are reduced by the shield, thereby reducing eddy source strength close to the exit plane. The reduction in shielded velocity gradient, however, lengthens the jet plume, and this reduction in turn leads to low-frequency amplification, as particularly noted for the suppressor configuration. The TAS impacts acoustic source modification more effectively for the 32-chute suppressor than for the annular plug nozzle, as evidenced by the noise reduction due to TAS at  $\theta_i = 90^\circ$  in figure 42. This suppression is another indication that TAS is more effective on noise sources located closer to the jet exit plane. The increased effectiveness on high-frequency jet noise sources also implies a significant reduction in mean velocity gradient, and this reduction in turn results in significant growth of the plume and causes low-frequency amplification.



(a) Semiannular ( $180^\circ$ ) shield.



(b) Annular ( $360^\circ$ ) shield.

Figure 41. Schematics of  $180^\circ$  and  $360^\circ$  thermal acoustic shield nozzles on circular jet. (From ref. 29.)

Figure 43 shows the influence of a  $180^\circ$  TAS on an annular plug nozzle and on a 32-chute suppressor nozzle in terms of PNL directivity. A 2.5-dB reduction in peak PNL levels and a 4-dB reduction in PNL are shown for the front quadrant of the annular plug nozzle with the TAS. For the 32-chute suppressor nozzle with the TAS, an 8-dB reduction in peak PNL and slightly less than an 8-dB reduction in PNL for the front quadrant are shown. These reductions indicate significantly more noise suppression obtained by the TAS on multielement suppressor nozzles than on the annular plug nozzles.

General experimental trends that evolved from the TAS studies (refs. 29 and 33) are as follows:

1. Partial shields yield higher noise reduction than full shields.
2. Increasing the thickness of the shield increases the noise reduction.
3. Noise reduction potential of TAS reduces as the core jet velocity increases above 671 m/sec (2200 ft/sec) for annular plug nozzles and above 732 m/sec (2400 ft/sec) for chute suppressor nozzles.
4. The TAS yields higher PNL reductions for multielement suppressor nozzles than for annular plug nozzles.

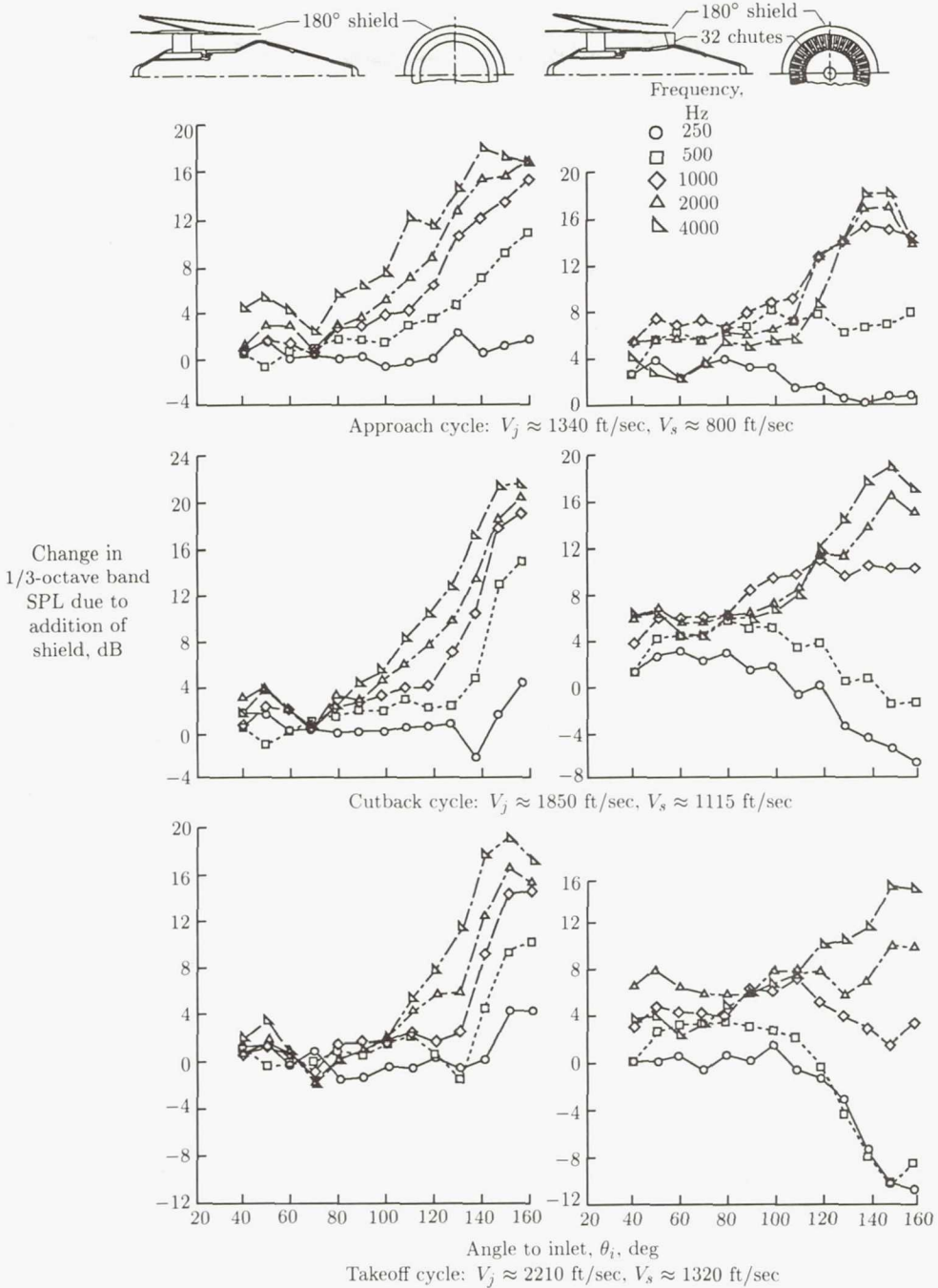


Figure 42. Influence of 180° TAS (0.97 in. thick) on directivity of various 1/3-octave bands for unsuppressed and mechanically suppressed annular plug nozzles.  $A_T = 1400 \text{ in}^2$ ; static operation. (From ref. 33.)

A TAS system can be implemented through various techniques, the end requirement being a stream of heated gas or air to surround the noisy jet. One method of implementation is to derive the TAS by bleeding the high-temperature gas from the main jet and throttling it through choke plates to reduce jet velocity and achieve a shield to the main jet velocity ratio of  $\approx 0.4$  to  $0.6$ . This shield removes the energy from the main jet, so the engine throttle must be advanced to compensate for thrust loss. For AST engines this would be feasible, as they are normally sized by thrust requirements at operation points other than the takeoff condition (e.g., cruise).

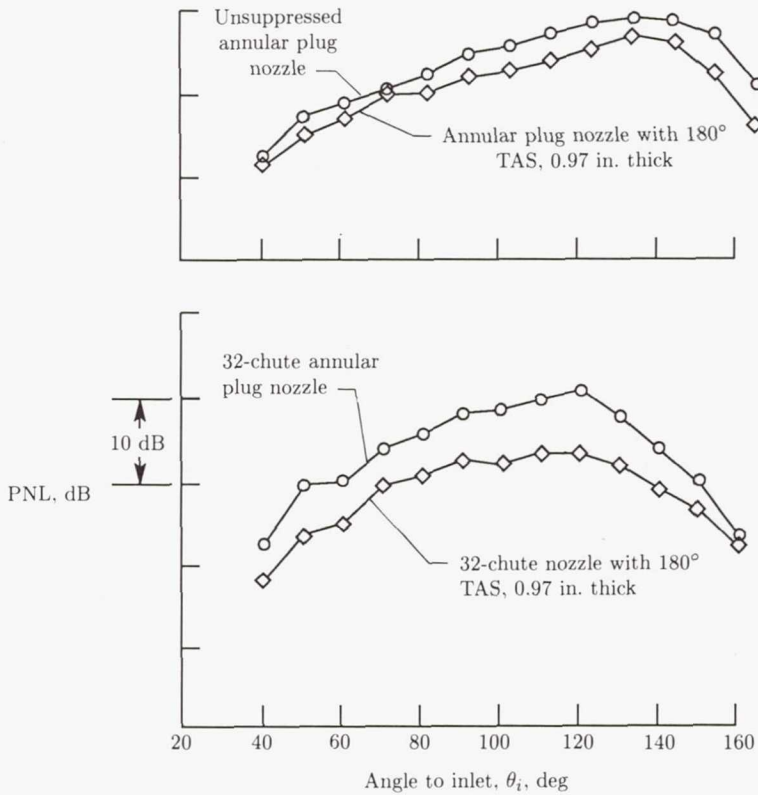


Figure 43. Influence of TAS on PNL directivity of unsuppressed annular plug and 32-chute suppressed nozzles at cutback cycle.  $A_T = 1400 \text{ in}^2$ ; 1000-ft flyover distance; static operation. (Based on ref. 33.)

Impact of a bleed-flow-type TAS was evaluated in an implementation study (ref. 33; see fig. 44). When thrust loss incurred by the bleed system is compensated for, the  $180^\circ$  TAS applied to the annular plug nozzle negates the benefit of the plug nozzle compared with the conical nozzle. Adding the  $180^\circ$  TAS to the 32-chute suppressor results in some benefit, even with the thrust loss, at lower thrust levels and results in some loss of benefit at the higher thrust levels. The study pointed out that a bleed-type system for TAS implementation would be of limited value.

An alternate method is to supply the TAS from an independent source of hot gas. This would add thrust to the overall system instead of degrading thrust by bleeding and would allow the main jet to be throttled back to a lower noise level thrust setting

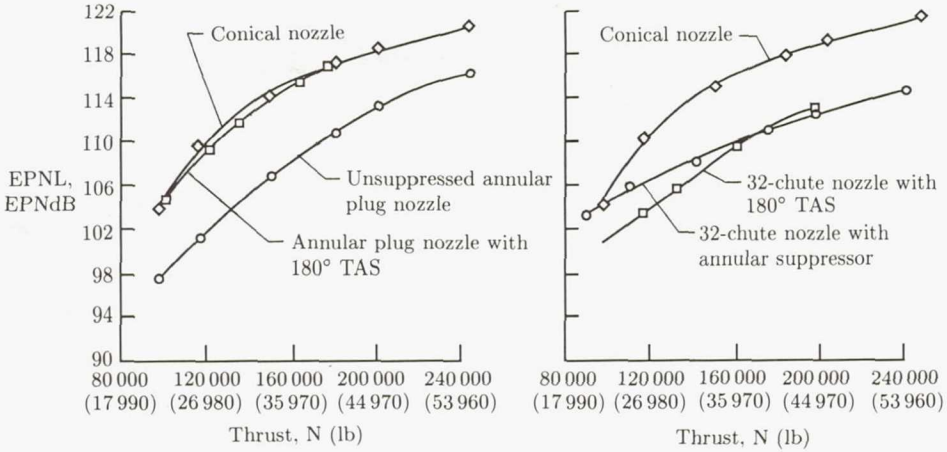


Figure 44. Integration study results of TAS implementation by bleeding. 305-m (1000-ft) level flyover at  $V = 122$  m/sec (400 ft/sec). (From ref. 33.)

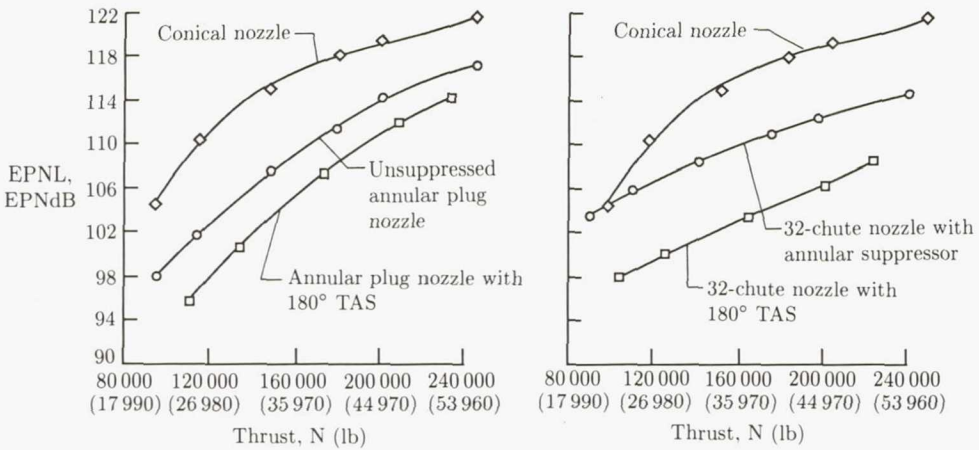


Figure 45. Integration study results of TAS implementation by independent source for shield flow. 305-m (1000-ft) level flyover at  $V = 122$  m/sec (400 ft/sec). (From ref. 33.)

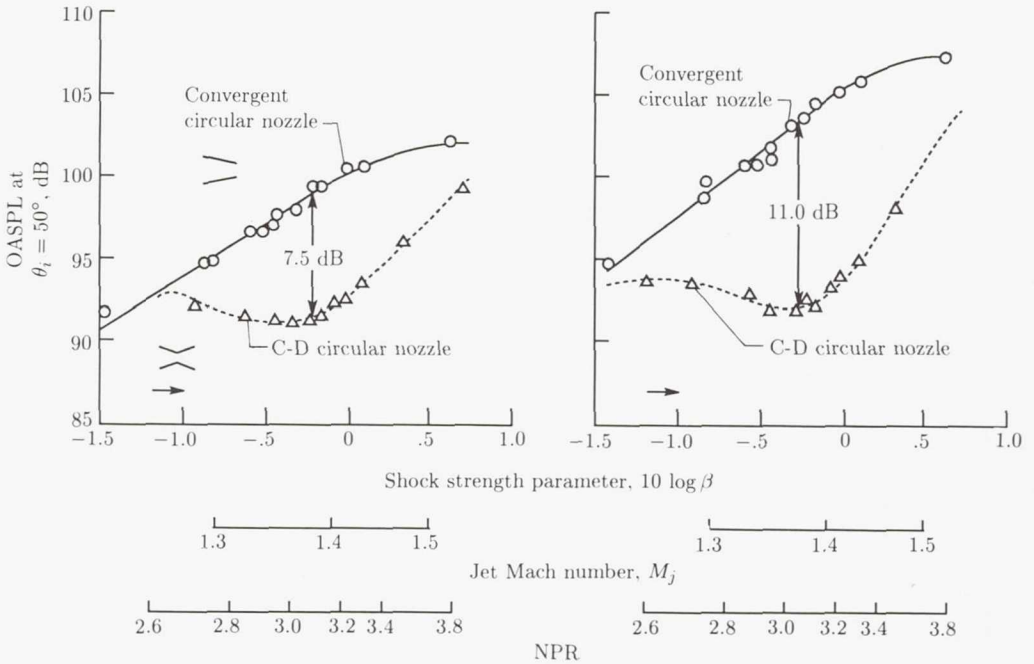
for takeoff. As noted from the results of the AST implementation study (ref. 33) presented in figure 45, this type of system has very significant advantages. For the 32-chute suppressor, jet noise levels are lowered to the point where other engine noise sources for an AST system could become the dominant noise source. A substantial effort is needed to cleverly implement an independent source of TAS that would not impose excessive weight and drag penalties.

### Shock Noise Control

Shock-cell broadband noise can be a significant contributor to the total noise radiated by jets operating at supercritical pressure ratios, particularly in the forward

quadrant, where jet mixing noise is lower. Experimental observations (refs. 9, 34, and 35) indicate that the shock-cell broadband noise is amplified in the forward quadrant due to flight. Nonisentropically expanded supersonic jets contain shock-cell structures which are formed from oblique compression and expansion waves for significant lengths of the jet plume, which is the physical means by which the static pressure balance is achieved between the jet and the ambient air. Interaction of turbulent eddies of the jet with the shock-cell structure results in acoustic waves termed shock-cell broadband noise. Shock noise control is obtained essentially by either eliminating or weakening the shock-cell structure by

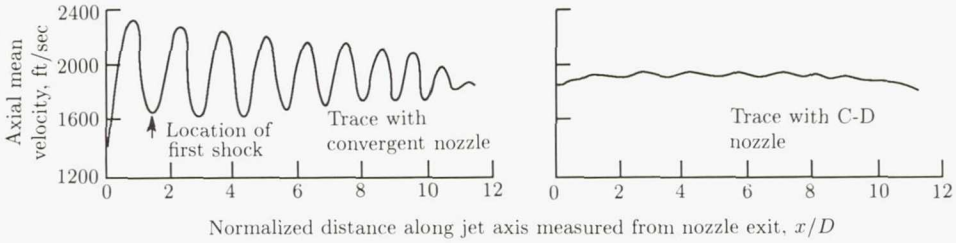
1. Aerodynamic design of the convergent-divergent (C-D) nozzle flow path
2. Plug structure modification for annular and dual-flow coannular plug nozzles
3. Proper choice of pressure ratios for operation of dual-flow nozzles



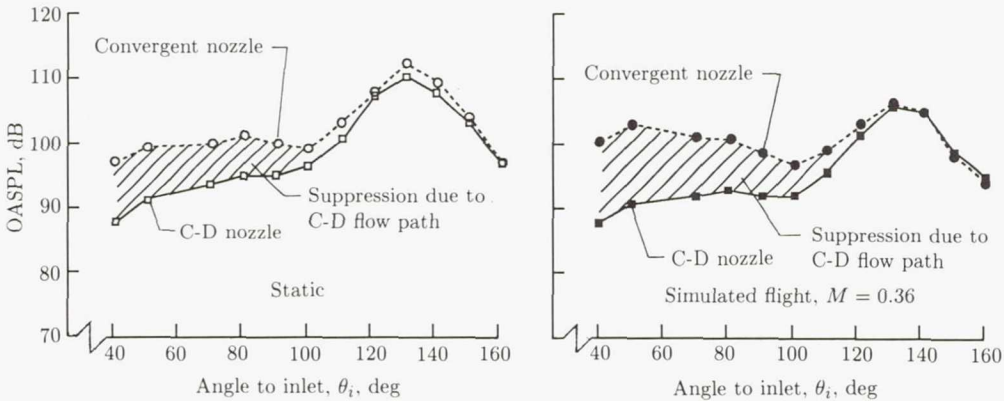
(a) Effectiveness of C-D flow path on circular nozzle in reduction of shock-cell noise. Data scaled to  $A_T = 1400 \text{ in}^2$  and extrapolated to 2400-ft sideline;  $T_T = 1700^\circ \text{R}$ .

Figure 46. Shock-cell noise reduction of C-D nozzle and of convergent circular nozzle. (From ref. 36.)

For the simple circular nozzle, the convergent-divergent design for isentropic flow expansion can be employed to eliminate the shock-cell structure in the jet at the design Mach number and thereby obtain shock noise reduction. Figure 46(a) (from ref. 36) shows the region of effectiveness of a circular C-D nozzle and of a convergent circular nozzle in controlling shock noise at and in the vicinity of the design Mach number of 1.4 (at a ratio of total to static pressure of 3.12 and a total temperature of 944 K (1700°R)). The OASPL reductions of 7.5 and 11.0 dB for a circular C-D nozzle are shown at the design condition for static and simulated flight at  $M = 0.36$ . Jet plume velocity data (fig. 46(b)) measured with a laser doppler velocimeter show the absence of the shock-cell structure for the C-D circular nozzle along the nozzle centerline at the design condition, whereas the convergent circular nozzle shows significant shock-cell structure at the same condition. The OASPL directivities shown in figure 46(c) indicate significant noise reduction in the forward quadrant obtained with the C-D circular nozzle for both static and simulated flight conditions.



(b) Plume velocity data for conical and C-D nozzles.  $V = 400$  ft/sec;  $T_T = 1720^\circ R$ ;  $NPR = 3.12$ .

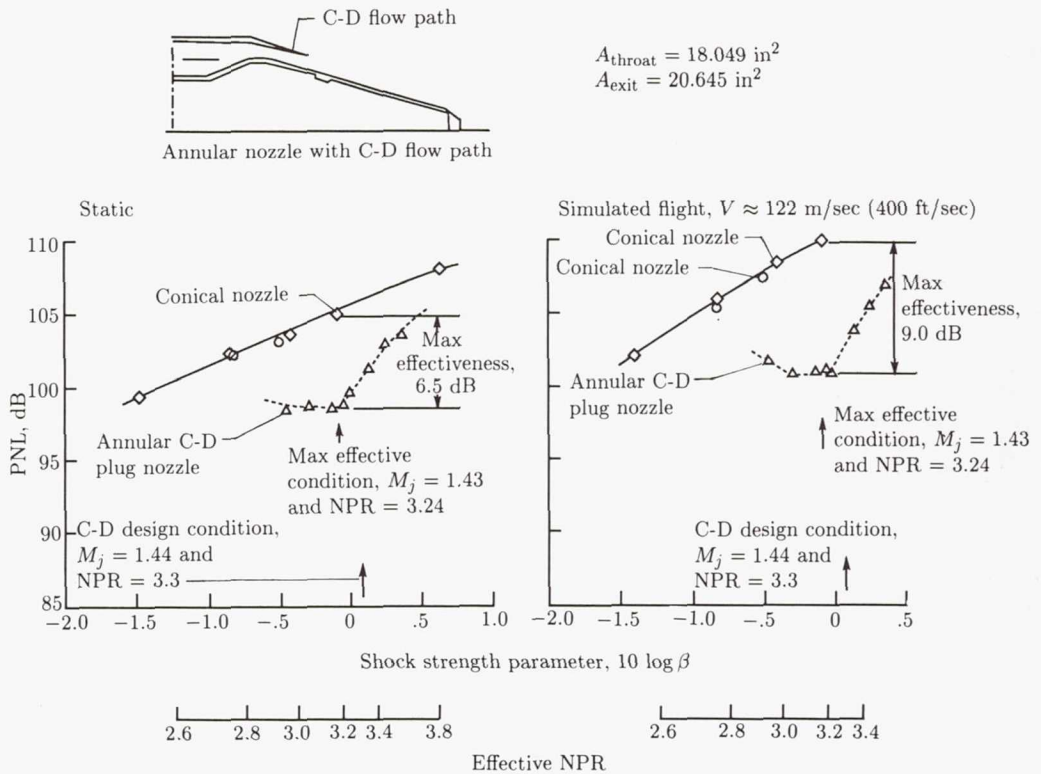


(c) OASPL directivity of convergent and C-D nozzles at C-D nozzle design conditions.

Figure 46. Concluded.

Next, the application of shock noise control techniques for annular and dual-flow coannular plug nozzles is discussed. When nozzles employing truncated plugs (i.e., plugs with a finite base area) are operated at highly underexpanded conditions, the jet plume has two shock-cell structures, one on the plug surface and one downstream of the truncated plug. The reason for two structures is that at highly underexpanded conditions, the shock-cell structure on the plug has not been able to slow the jet plume to subsonic conditions at the end of the plug. As the supersonic jet expands over the truncated plug, an expansion fan is created which reflects off the jet shear layer as an oblique shock which in turn sets up an expansion fan, and so on. This process results in another shock-cell structure downstream of the plug. Hence, shock noise control for nozzles employing plugs must address elimination or mitigation of both the shock-cell structures.

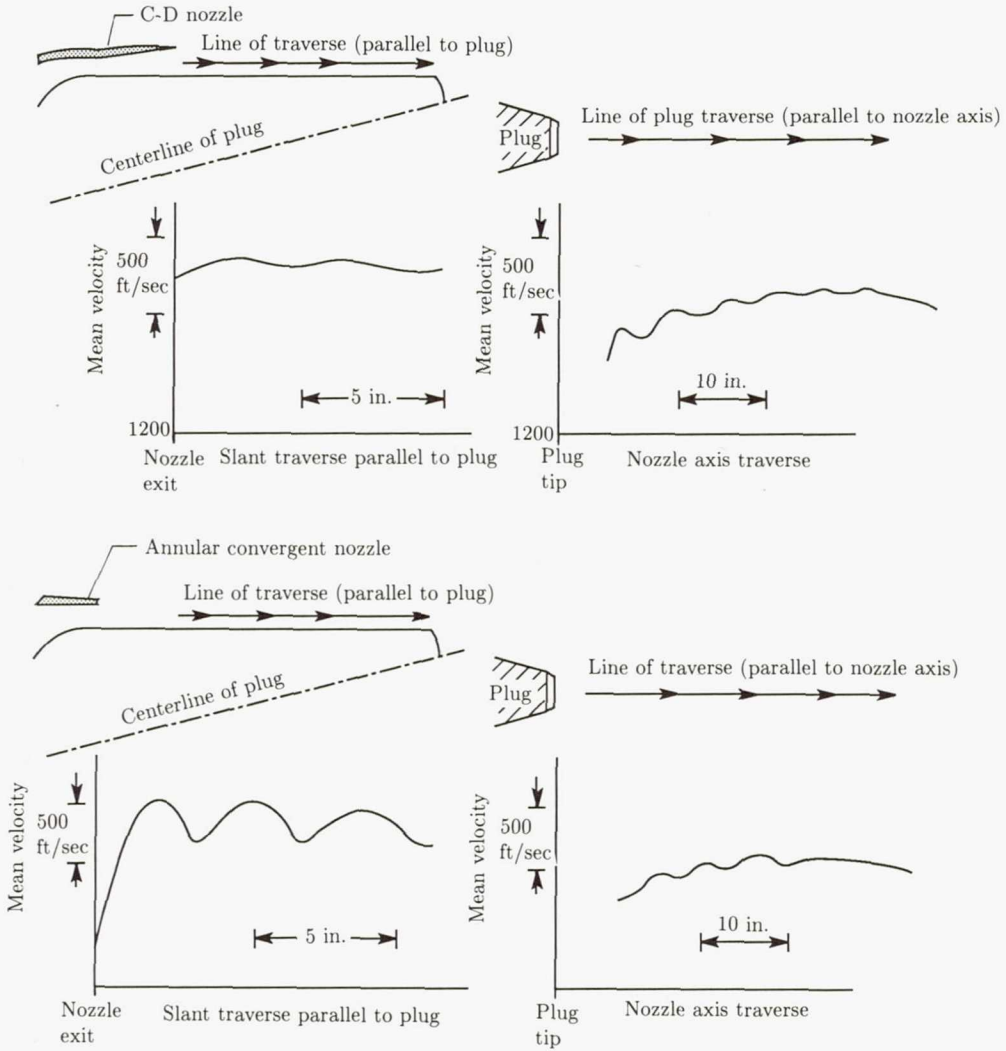
Figure 47(a) (from ref. 36) indicates the effectiveness of a C-D flow path in reducing shock noise for an annular plug nozzle with a truncated plug at or near the design Mach number of 1.44 for both static and simulated flight conditions. Jet plume velocity data both along the plug surface and downstream of the truncated



(a) Effectiveness of C-D flow path in shock noise reduction for annular plug nozzle in terms of PNL at  $\theta_i = 60^\circ$ . Data scaled to  $A_T = 0.903 \text{ m}^2$  ( $1400 \text{ in}^2$ ) and 732-m (2400-ft) sideline.

Figure 47. Shock noise reduction for annular plug nozzle with C-D nozzle flow path. (From ref. 36.)

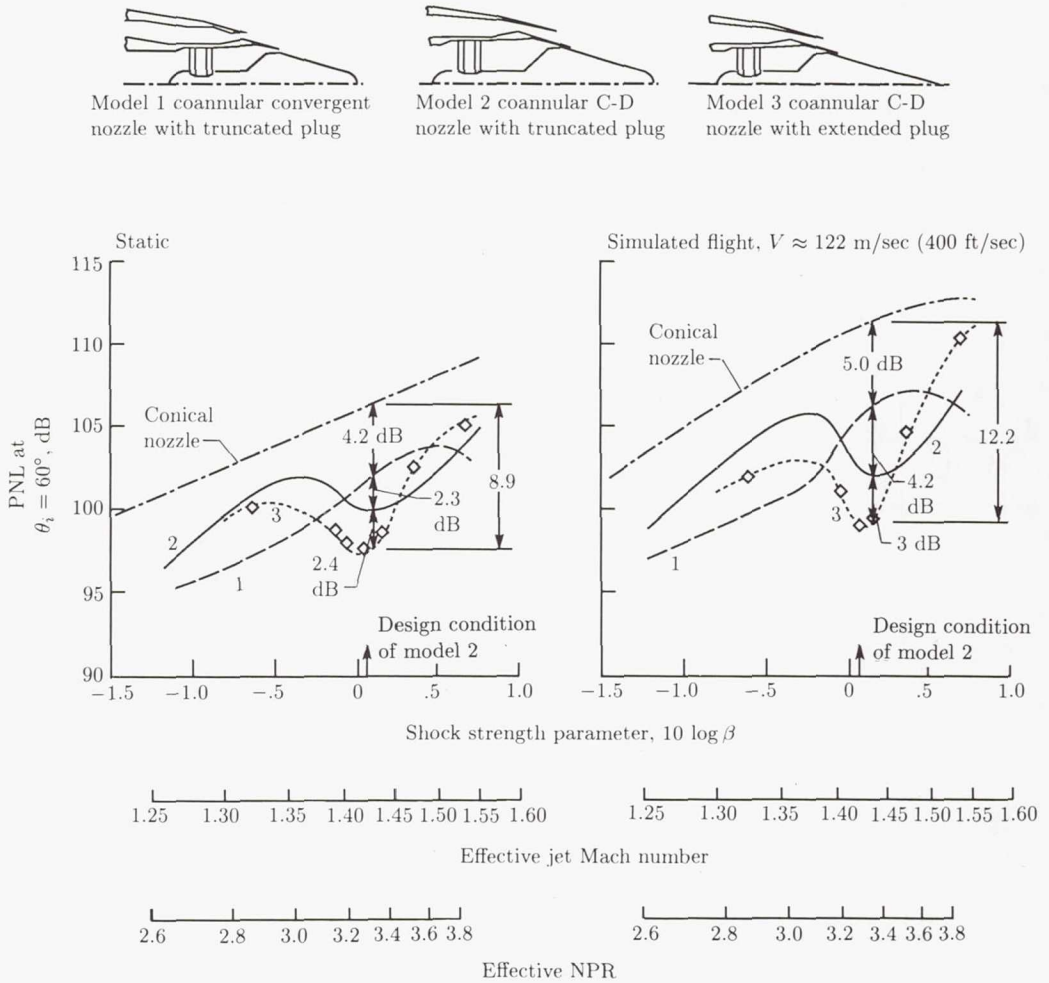
plug at the design Mach number are shown in figure 47(b). The C-D flow path for the annular passage eliminates the shock-cell structure along the plug surface, whereas both the convergent and C-D annular plug nozzles have shock-cell structures downstream of the plug. Since this design did not eliminate both the shock-cell structures, the shock noise control effectiveness of the C-D annular plug nozzle is less than that of the circular C-D nozzle (compare figs. 46(a) and 47(a)).



(b) Mean velocity data for C-D annular plug nozzle operating at its design condition.

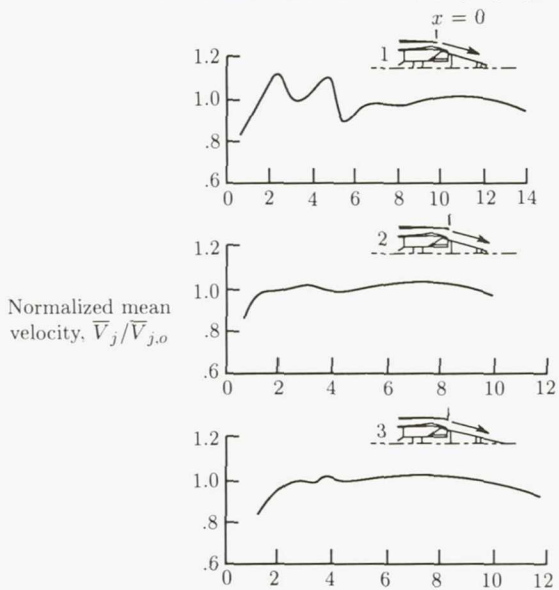
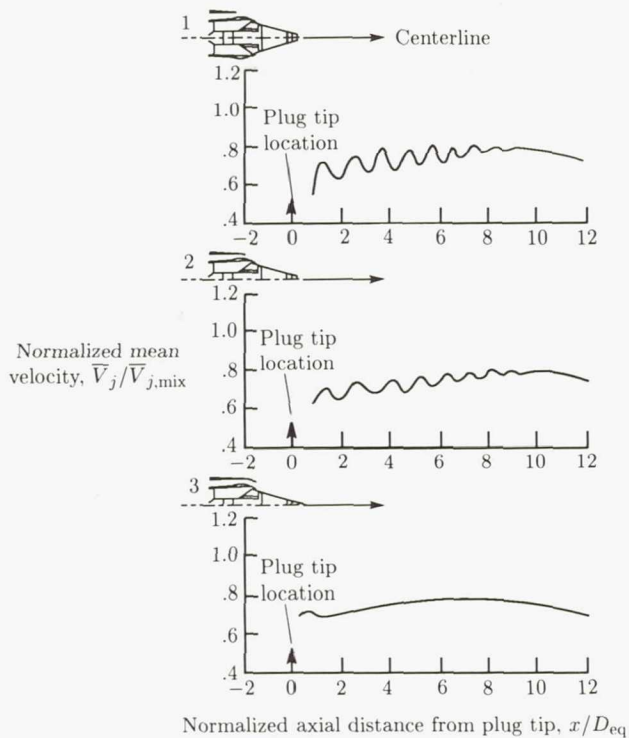
Figure 47. Concluded.

Shock noise control techniques for dual-flow coannular plug nozzles with inverted velocity profiles are now examined. Figure 48 summarizes the results of shock noise control for dual-flow coannular plug nozzles with C-D flow paths for both inner and outer streams having design Mach numbers of 1.38 and 1.44, respectively. The area ratio of inner stream to outer stream is 0.2. Model 1 employs convergent flow paths



(a) Effectiveness of shock-cell noise reduction for coannular nozzles.

Figure 48. Shock noise reduction for coannular plug nozzle with C-D flow path and plug tip modification. (Based on ref. 36.)



(b) Mean velocity distributions.

Figure 48. Concluded.

for both the streams and a truncated plug. Model 2 employs C-D flow paths for both the streams and a truncated plug, and Model 3 employs C-D flow paths for both the streams and a sharp-tipped plug (i.e., no base region for the plug). Application of C-D flow paths reduces the noise levels at and near the design condition. (See figure 48(a).) The application of a sharp-tipped plug reduces the shock noise further and yields about the same total effectiveness relative to the circular convergent nozzle as does the circular C-D nozzle. The jet plume traces for models 1, 2, and 3 at the design condition indicate the absence of shocks on the plug for models 2 and 3, and this absence is a direct consequence of the C-D flow path. The sharp-tipped plug eliminates shock-cell structure downstream of the plug because of the absence of the expansion fan at the plug tip. (See fig. 48(b).)

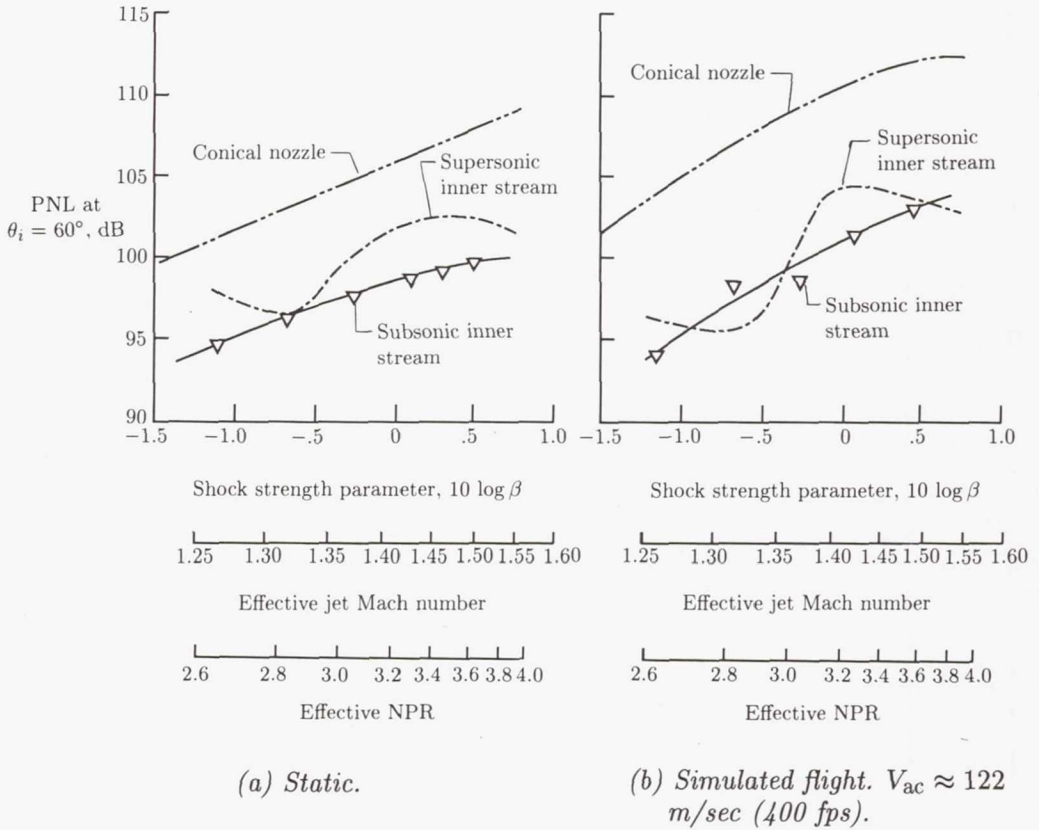
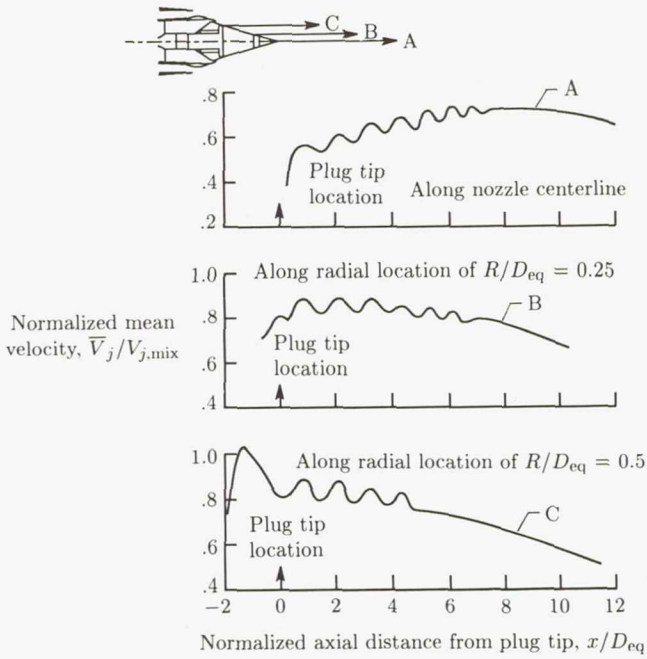
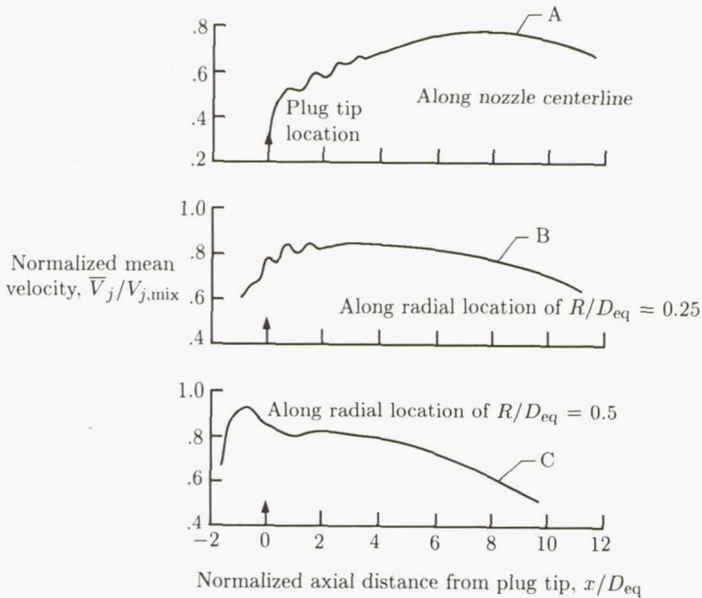


Figure 49. Effectiveness of subsonic inner stream operation on shock noise of coannular extended plug nozzle. Data scaled to  $A_T = 0.903 \text{ m}^2$  ( $1400 \text{ in}^2$ ) and 732-m (2400-ft) sideline. (Based on ref. 36.)

An effective means of flow management and resultant shock structure control for the dual-flow coannular plug nozzles is obtained by operating the inner stream at subcritical pressure ratios. Figure 49 shows the shock noise characteristics obtained with the inner nozzle operated at a fixed pressure ratio of 1.80 for subsonic operation and



(a) Supersonic inner stream;  $NPR_i = 3.14$ ;  $NPR_o = 3.33$ ;  $T_{T,i} = 870^\circ R$ ;  $T_{T,o} = 1670^\circ R$ .



(b) Subsonic inner stream;  $NPR_i = 1.80$ ;  $NPR_o = 3.32$ ;  $T_{T,i} = 1280^\circ R$ ;  $T_{T,o} = 1695^\circ R$ .

Figure 50. Axial mean velocity distribution of convergent coannular plug nozzle with supersonic and subsonic inner streams. (From ref. 36.)

3.13 for supersonic operation over a range of outer nozzle pressure ratios of 2.5 to 4.0. Significant shock noise reduction is found at *all* conditions with the subsonic inner stream. The subsonic inner stream significantly alters the shock structure downstream of the plug, as indicated by the velocity measurements shown in figure 50, which are indicative of reduced shock-cell noise.

As mentioned previously, multielement suppressors have significantly lowered shock-cell noise because of the associated rapid mixing and shock-cell structure decay and the relatively high frequencies of shock noise of individual elements, which are effectively attenuated by atmospheric absorption. However, if additional shock noise reduction is required, individual elements (such as chutes or spokes) may be designed to have C-D flow paths. (See refs. 36 and 37 for multielement suppressor nozzles with dual- and single-flow applications, respectively.)

Another approach for shock noise control is the porous plug concept, initially proposed by Maestrello (ref. 38). The application of a porous plug, either sealed or vented to the atmosphere, replaces the periodic shock-cell structure noted for nonporous plugs with a series of weak compression waves which yield shock-cell noise reduction.

Of further concern may be shock screech noise. Shock screech noise was first studied by Powell (ref. 39), who proposed the existence of a feedback mechanism between the nozzle exit and the shock cells via the upstream propagation of the acoustic wave generated at the shock cell through the subsonic mixing layer of the jet and reinforcing the feedback loop. Shock screech noise, unlike shock-cell broadband noise, has a pure tone characteristic and can lead to sonic fatigue of the nozzle hardware because of the relatively high levels. Methods employed to reduce the amplitude of shock screech noise are aimed at destroying the feedback loop by causing perturbations in the flow near the nozzle exit plane (e.g., screech tabs or nozzle exit plane roughness).

## Summary

The objectives of this chapter were to review and summarize the jet noise suppression technology, to provide a physical and theoretical model to explain the measured jet noise suppression characteristics of different concepts, and to provide a set of "guidelines" for evolving jet noise suppression designs. The underlying principle for all the jet noise suppression devices is to enhance rapid mixing (i.e., diffusion) of the jet plume by geometric and aerothermodynamic means. In the case of supersonic jets, the shock-cell broadband noise reduction is effectively accomplished by the elimination or mitigation of the shock-cell structure. So far, the diffusion concepts have predominantly concentrated on jet momentum and energy (kinetic and thermal) diffusion, in that order, and have yielded better noise reduction than the simple conical nozzle.

However, these noise reductions are not large enough to guarantee compliance with noise regulations for engines being considered for high-speed applications, such as HSCT's. The current trend is toward higher jet velocities, so that engine size (and hence vehicle takeoff gross weight) will be smaller for a given sea level static thrust requirement. This trend presents tougher challenges for the scientific and technical community to reduce the jet noise at these higher jet velocities. This situation will call for innovative concepts for jet noise reduction. One avenue which has not been

vigorously pursued so far is diffusion concepts which employ concentration gradients of different species in addition to velocity and temperature gradients.

A critical technology issue that needs resolution is the effect of flight on the noise suppression potential of mechanical suppressor nozzles. Scale-model test data in simulated flight and limited flight-test data indicate that the noise suppression potential of mechanical suppressor nozzles over an equivalent conical nozzle deteriorates in flight whereas it does not in the static case. A more thorough investigation of this mechanism is necessary for the successful development and design of an acceptable noise suppression device for future HSCT's.

## References

1. Lush, P. A.: Measurements of Subsonic Jet Noise and Comparison With Theory. *J. Fluid Mech.*, vol. 46, pt. 3, Apr. 1971, pp. 477-500.
2. Cocking, B. J.: *The Effect of Temperature on Subsonic Jet Noise*. R. & M. No. 3771, British Aeronautical Research Council, 1975. (Supersedes NGTE Rep. 331.)
3. Mani, R.: The Jet Density Exponent Issue for the Noise of Heated Subsonic Jets. *J. Fluid Mech.*, vol. 64, pt. 3, July 8, 1974, pp. 611-622.
4. Mani, R.: The Influence of Jet Flow on Jet Noise. *J. Fluid Mech.*, vol. 73, pt. 4, Feb. 24, 1976. Part 1: The Noise of Unheated Jets, pp. 753-778. Part 2: The Noise of Heated Jets, pp. 779-793.
5. Balsa, Thomas F.: The Far Field of High Frequency Convected Singularities in Sheared Flows, With an Application to Jet-Noise Prediction. *J. Fluid Mech.*, vol. 74, pt. 2, Mar. 23, 1976, pp. 193-208.
6. Lilley, G. M.; Morris, P.; and Tester, B. J.: On the Theory of Jet Noise and Its Applications. AIAA Paper No. 73-987, Oct. 1973.
7. Ribner, H. S.: Quadrupole Correlations Governing the Pattern of Jet Noise. *J. Fluid Mech.*, vol. 38, pt. 1, Aug. 14, 1969, pp. 1-24.
8. Goldstein, Marvin E.: *Aeroacoustics*. NASA SP-346, 1974.
9. Balsa, T. F.; Glibe, P. R.; Kantola, R. A.; Mani, R.; Stringas, E. J.; and Wang, J. C. F.: *High Velocity Jet Noise Source Location and Reduction. Task 2—Theoretical Developments and Basic Experiments*. FAA-RD-76-79, II, May 1978. (Available from DTIC as AD A094 291.)
10. Balsa, Thomas F.; and Glibe, Philip R.: Aerodynamics and Noise of Coaxial Jets. *AIAA J.*, vol. 15, no. 11, Nov. 1977, pp. 1550-1558.
11. Glibe, Philip R.; and Balsa, Thomas F.: Aeroacoustics of Axisymmetric Single- and Dual-Flow Exhaust Nozzles. *J. Aircr.*, vol. 15, no. 11, Nov. 1978, pp. 743-749.
12. Glibe, P. R.: Diagnostic Evaluation of Jet Noise Suppression Mechanisms. *J. Aircr.*, vol. 17, no. 12, Dec. 1980, pp. 837-842.
13. Harper-Bourne, M.; and Fisher, M. J.: The Noise From Shock Waves in Supersonic Jets. *Noise Mechanisms*, AGARD-CP-131, Mar. 1974, pp. 11-1-11-13.
14. Grose, R. D.; and Kendall, R. M.: Theoretical Predictions of the Sound Produced by Jets Having an Arbitrary Cross Section. *ASME Symposium on Fully Separated Flows*, 1964, pp. 58-63.
15. Davies, P. O. A. L.; Fisher, M. J.; and Barratt, M. J.: The Characteristics of the Turbulence in the Mixing Region of a Round Jet. *J. Fluid Mech.*, vol. 15, pt. 3, Mar. 1963, pp. 337-367.
16. Stone, James R.: *Supersonic Jet Shock Noise Reduction*. NASA TM-83799, 1984.
17. Brausch, J. F.; and Doyle, V. L.: *Supersonic Transport Noise Reduction Technology Summary, Phase I. Summary of GE4/SST Acoustic Suppression Research, Volume 1*. Rep. No. FAA-SS-72-42, Vol. I, Dec. 1972.

18. Shields, F. Douglas; and Bass, H. E.: *Atmospheric Absorption of High Frequency Noise and Application to Fractional-Octave Bands*. NASA CR-2760, 1977.
19. *American National Standard Method for the Calculation of the Absorption of Sound by the Atmosphere*. ANSI S1.26-1978 (ASA 23-1978), American National Standards Inst., Inc., June 23, 1978.
20. Brausch, J.; Clapper, W. S.; Gliebe, P. R.; Lee, R.; Whittaker, R.; Mani, R.; Motsinger, R. E.; Schloemer, J.; Sieckman, A.; and Stringas, E. J.: *High Velocity Jet Noise Source Location and Reduction. Task 6: Noise Abatement Nozzle Design Guide*. FAA-RD-76-79-6, Apr. 1979. (Available from DTIC as AD A103 671.)
21. Baumgardt, N.; Brausch, J.; Clapper, W. S.; Mani, R.; Stringas, E. J.; Vogt, P.; and Whittaker, R.: *High Velocity Jet Noise Source Location and Reduction. Task 5: Investigation of In-Flight Aeroacoustic Effects on Suppressed Exhausts*. FAA-RD-76-79-5, Jan. 1979. (Available from DTIC as AD A094 297.)
22. Eldred, Kenneth M.; White, Robert W.; Mann, Myron A.; and Cottis, Miltiades G.: *Suppression of Jet Noise With Emphasis on the Near Field*. ASD-TDR-62-578, U.S. Air Force, Feb. 1963.
23. Brooks, J. R.; McKinnon, R. A.; and Johnson, E. S.: Results From Flight Noise Tests on a Viper Turbojet Fitted With Ejector/Suppressor Nozzle Systems. AIAA-80-1028, June 1980.
24. Blozy, J. T.; Doyle, V. L.; Kazin, S. B.; Mishler, R. B.; Nebuda, R. L.; Stringas, E. J.; and Sieckman, A. R.: *Supersonic Transport Noise Reduction Technology Program—Phase 2*. Sept. 1975.  
Volume 1, FAA-SS-73-29-1-VOL-1. (Available from DTIC as AD B010 468L.)  
Volume 2, FAA-SS-73-29-1-VOL-2. (Available from DTIC as AD B010 469L.)
25. Brausch, J. F.; Motsinger, R. E.; and Hoerst, D. J.: *Simulated Flight Acoustic Investigation of Treated Ejector Effectiveness on Advanced Mechanical Suppressors for High Velocity Jet Noise Reduction*. NASA CR-4019, 1986.
26. Brausch, J. F.; Clapper, W. S.; Scott, P. F.; Smith, M. A.; Stringas, E. J.; and Whittaker, R. W.: *High Velocity Jet Noise Source Location and Reduction. Task 3—Experimental Investigation of Suppression Principles, Volume II—Parametric Testing and Source Measurements*. Rep. No. FAA-RD-76-79, III-II, Dec. 1978. (Available from DTIC as AD A094 294.)
27. Vdoviak, John W.; Knott, Paul R.; and Ebacker, Jon J.: *Aerodynamic/Acoustic Performance of YJ101/Double Bypass VCE With Coannular Plug Nozzle*. NASA CR-159869, 1981.
28. Kozlowski, Hilary; and Packman, Allan B.: *Aerodynamic and Acoustic Tests of Duct-Burning Turbofan Exhaust Nozzles*. NASA CR-2628, 1976.
29. Janardan, B. A.; Brausch, J. F.; and Majjigi, R. K.: *Free Jet Feasibility Study of a Thermal Acoustic Shield Concept for AST/VCE Application—Dual Stream Nozzles*. NASA CR-3867, 1985.
30. Ahuja, K. K.; and Dosanjh, D. S.: Heated Fluid Shroud as an Acoustic Shield for Noise Reduction—An Experimental Study. AIAA Paper 77-1286, Oct. 1977.
31. Goodykoontz, J.: *Effect of a Semi-Annular Thermal Acoustic Shield on Jet Exhaust Noise*. NASA TM-81615, 1980.
32. Pickup, N.; Mangiarotty, R. A.; and O'Keefe, J. V.: Tests of a Thermal Acoustic Shield With a Supersonic Jet. AIAA-81-2021, Oct. 1981.
33. Majjigi, R. K.; Brausch, J. F.; Janardan, B. A.; Balsa, T. F.; Knott, P. R.; and Pickup, N.: *Free Jet Feasibility Study of a Thermal Acoustic Shield Concept for AST/VCE Application—Single Stream Nozzles*. NASA CR-3758, 1984.
34. Sarohia, V.: Some Flight Simulation Experiments on Jet Noise From Supersonic Under-expanded Flows. *AIAA J.*, vol. 16, no. 7, July 1978, pp. 710-716.
35. Yamamoto, K.; Brausch, J. F.; Janardan, B. A.; Hoerst, D. J.; Price, A. O.; and Knott, P. R.: *Experimental Investigation of Shock-Cell Noise Reduction for Single-Stream Nozzles in Simulated Flight. Comprehensive Data Report*. 1984.  
Volume I, Test Nozzles and Acoustic Data, NASA CR-168234-VOL-I.

*Volume II, Laser Velocimeter Data*, NASA CR-168234-VOL-II.

*Volume III, Shadowgraph Photos and Facility Description*, NASA CR-168234-VOL-III.

36. Janardan, B. A.; Yamamoto, K.; Majjigi, R. K.; and Brausch, J. F.: *Experimental Investigation of Shock-Cell Noise Reduction for Dual-Stream Nozzles in Simulated Flight*. NASA CR-3846, 1984.
37. Yamamoto, K.; Brausch, J. F.; Balsa, T. F.; Janardan, B. A.; and Knott, P. R.: *Experimental Investigation of Shock-Cell Noise Reduction for Single Stream Nozzles in Simulated Flight*. NASA CR-3845, 1984.
38. Maestrello, Lucio: *Initial Results of a Porous Plug Nozzle for Supersonic Jet Noise Suppression*. NASA TM-78802, 1978.
39. Powell, A.: On the Mechanism of Choked Jet Noise. *Proc. Phys. Soc. (London)*, Section B, vol. 66, pt. 12, 1953, pp. 1039-1056.